DIRECT TESTING OF FORSTERITE BICRYSTALS VIA *in-situ* MICROPILLAR EXPERIMENTS AT 700°C

Diana Avadanii[1], Lars Hansen[2], Ed Darnbrough[3], Katharina Marquardt[4], David Armstrong[3], and Angus Wilkinson[3]

[1]Department of Earth Sciences, University of Oxford

[2]Department of Earth and Environmental Sciences, University of Minnesota

[3]Department of Materials, University of Oxford

[4]Department of Materials, Imperial College London

Word count including title, headings, figure captions, and text: 8003

ABSTRACT

The mechanics of olivine deformation play a key role in long-term planetary processes, including the response of the lithosphere to tectonic loading or the response of the solid Earth to tidal forces, and in short-term processes, such as post-seismic creep within the upper mantle. Previous studies have emphasized the importance of grain-size effects in the deformation of olivine. Most of our understanding of the role of grain boundaries in the deformation of olivine is inferred from comparison of experiments on single crystals to experiments on polycrystalline samples, as there are no direct studies of the mechanical properties of individual grain boundaries in olivine. In this study, we use high-precision mechanical testing of synthetic forsterite bicrystals with well characterized interfaces to directly observe and quantify the mechanical properties of olivine grain boundaries. We conduct *in-situ* micropillar compression tests at high-temperature (700°C) on bicrystals containing low-angle (4° tilt about [100] on (014)) and high-angle (60° tilt about [100] on (011)) boundaries. During the *in-situ* tests, we observe differences in deformation style between the pillars containing the grain boundary and the pillars in the crystal interior. In the pillars containing the grain boundary, the interface is oriented at $\sim 45°$ to the loading direction to promote shear. *In-situ* observations and analysis of the mechanical data indicate that pillars containing the grain boundary consistently support elastic loading to higher stresses than the pillars without a grain boundary. Moreover, the pillars without the grain boundary sustain larger plastic strain. Post-deformation microstructural characterization confirms that under the conditions of these deformation experiments, sliding did not

occur along the grain boundary. These observations support the hypothesis that grain boundaries are stronger relative to the crystal interior at these conditions.

Keywords olivine deformation · grain-boundary micromechanics · in-situ micropillar deformation

1 Introduction

The rheological behavior of olivine at the thermo-mechanical conditions of Earth's upper mantle has been the focus of a number of studies. Laboratory experiments provide insight into olivine deformation under a wide range of conditions and form the basis for calibrating flow laws for extrapolation to geological conditions [e.g., Hirth and Kohlstedt, 2003]. However, predictions of the mechanical properties of the lithosphere based on laboratory results are inconsistent and also disagree with estimates based on geophysical observations [e.g., Hunter and Watts, 2016, Zhong and Watts, 2013, Hansen et al., 2019, Karato, 2010].

One challenge associated with laboratory studies at elevated temperatures and pressures relevant to the upper mantle is separating and quantifying the role of different variables (e.g., oxygen fugacity, starting microstructure, trace elements [Hansen and Kohlstedt, 2015]) that simultaneously impact deformation [e.g., Thieme et al., 2018, Bollinger et al., 2019, Faul et al., 2011, Hansen and Kohlstedt, 2015]. Microstructural analysis is generally only performed after quenching and decompression and after additional sample preparation for the desired characterization technique. This *post-mortem* assessment has constrained previous studies to inference of the microphysical mechanisms of deformation rather than direct observation [e.g., Thieme et al., 2018, Hansen et al., 2012a, Tielke et al., 2016a]. However, this obstacle can be overcome by miniaturized mechanical testing at the micron scale, which facilitates the *in-situ* observation of material deformation [for a review, see Kacher et al., 2019], and the targeted investigation of key structural features such as grain boundaries.

Grain boundaries and their density (i.e., grain size) play a key role in ductile deformation of olivine under a wide range of conditions. At low temperatures and high stresses, permanent deformation is accommodated by dislocation generation and the glide of dislocations through the crystal lattice, as diffusion is inhibited [Ch 2, Frost and Ashby, 1982]. In olivine, this regime has been investigated in laboratory studies on single crystals [e.g., Kranjc et al., 2016, Demouchy et al., 2013, Evans and Goetze, 1979, Idrissi et al., 2016] and polycrystalline samples [e.g., Druiventak et al., 2011, Mei et al., 2010, Raterron et al., 2004, Faul et al., 2011] with little agreement among results. However, these past discrepancies have been reconciled by studies documenting a size effect during low-temperature plasticity of olivine [Kumamoto et al., 2017, Hansen et al., 2019, Koizumi et al., 2020]. Kumamoto et al. [2017] and Koizumi et al. [2020] used mechanical testing at a range of length scales in single crystals and Hansen et al. [2019] used measurements on polycrystalline samples with different grain sizes, all of whom documented a size effect in which permanent deformation at smaller length scales (or smaller grain sizes) requires higher stresses. Observations of stronger samples with decreasing grain size are attributed to the empirical Hall-Petch effect [Hall, 1951, Petch, 1953], a phenomenon widely documented in metals [for a review, see Cordero et al., 2016]. The microphysics of this effect

rely on the interactions between mobile lattice dislocations and grain boundaries [Cordero et al., 2016]. In olivine, inferences of these phenomena are based on *post-mortem* microscopy of deformed samples [e.g., Wallis et al., 2020].

At increased temperatures, diffusion enables the mobility of defects within the grain-boundary plane [Ashby, 1972]. Under an applied differential stress, grain boundaries start to slide, which can be accommodated by diffusion of vacancies, mobility of dislocations within the grain-boundary plane, or elastic processes [Ashby, 1972]. Grain-boundary sliding generates incompatibilities and stress concentrations in the crystal lattice, while relaxing the shear stresses within the grain-boundary plane. These stress gradients promote diffusion of material [Raj and Ashby, 1971, 1972, Ashby, 1972] or nucleation of lattice dislocations [Langdon, 2009]. In olivine, laboratory-based studies have inferred that grain-boundary sliding (GBS) in conjunction with motion of lattice dislocations (sometimes called dislocation-accommodated GBS) or diffusive mass transfer (sometimes called diffusion creep) becomes a dominant deformation mechanism in polycrystalline olivine at finer grain sizes [e.g., Hirth and Kohlstedt, 1995a,b, Hansen et al., 2011, Tielke et al., 2016b, Hansen and Kohlstedt, 2015, Yabe et al., 2020, Kim et al., 2022]. The details of the microphysical mechanisms operating during grain-boundary sliding in olivine remain unresolved across different deformation conditions [e.g., Hansen et al., 2011, Jackson et al., 2014, Tielke et al., 2016a]. This deformation mechanism is of particular importance to the rheology of the upper mantle as extrapolations of flow laws to geological conditions indicate that GBS is a dominant deformation mechanism in much of the upper mantle, where it contributes towards seismic anisotropy and strain accommodation [Hansen et al., 2011, 2012b, Ohuchi et al., 2015, Tielke et al., 2016b, Hansen and Kohlstedt, 2015]. Moreover, during diffusion creep, defect motion along grain boundaries could also impact rock properties deforming over short, transient periods [Jackson et al., 2014, Faul and Jackson, 2015]. Faul and Jackson [2015] highlight the importance of grain boundaries in seismic attenuation, and indicate that dislocation-related attenuation could also be of importance. Consequently, studies investigating strain accommodation in olivine have placed processes involving grain boundaries under increased significance [e.g., Samae et al., 2021, Bollinger et al., 2019, Sun et al., 2016, Jackson et al., 2014, Cordier et al., 2014, Gasc et al., 2019, Ferreira et al., 2021, Thieme et al., 2018].

Although significant advances have been made towards understanding the structure, composition, and chemistry of grain boundaries in olivine [for review, see Marquardt and Faul, 2018, Demouchy, 2021], we lack direct observations documenting the interactions between grain boundaries and crystal defects. In this study, we contribute towards filling this gap by deploying small-scale, uniaxial, *in-situ* mechanical testing on two pure forsterite (Fo) bicrystals. The experiments are performed at a temperature of 700°C with a sample orientation designed to maximise the resolved shear stress on the grain-boundary plane and promote grain-boundary sliding. Testing a pure Fo synthetic bicrystal allows us to remove the impact of prexisting defects and investigate a specific boundary of known character. This strategy of using bicrystals to probe interface properties has successfully been applied in a number of engineering materials [for a review, see Dehm et al., 2018]. In geological materials, studies using synthetic bicrystals reveal information on grain-boundary structure of specific configurations and grain-boundary diffusion rates [Polednia et al., 2020, Marquardt et al., 2011, Gardés et al., 2021]. Furthermore, increased capabilities for micromechanical testing at high-temperatures have enabled an increasing number of experiments on deformation of ceramic materials [for review, see Korte-Kerzel,

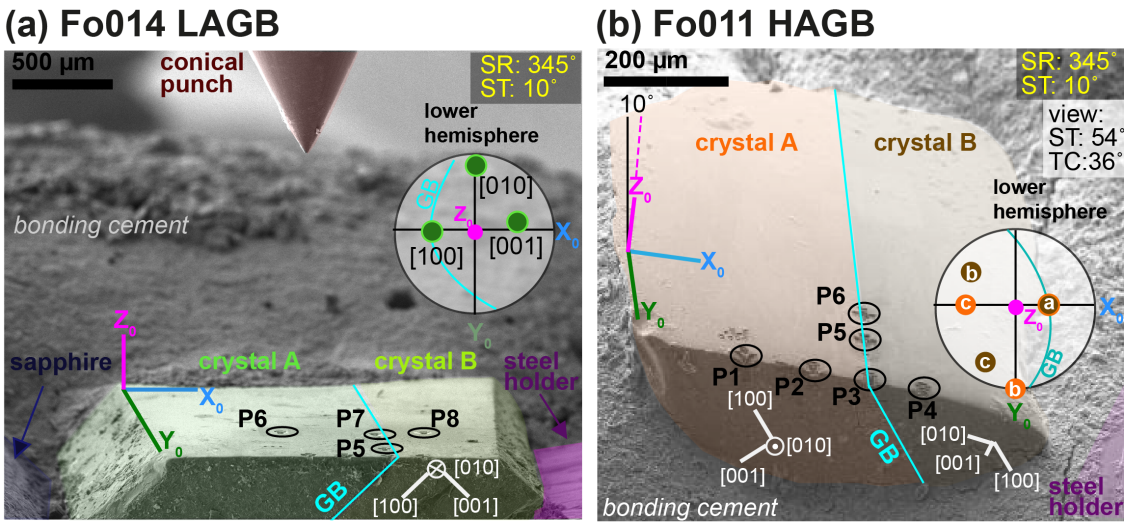

Figure 1: Sample assembly for the low-angle grain boundary in (a) and the high-angle grain boundary in (b). Panel a) is a colorised image of the low-magnification, *in-situ* view of the micropillars. The colored axes represent the sample surface coordinate convention. Panel b) is a colorised image of the high-angle grain boundary bicrystal assembly imaged with the stage tilt (ST) and tilt correction (TC) that display the least distortion along the Z_0 axis (i.e., parallel to the pillar vertical axis). The orientation of the samples is described using lower-hemisphere stereographic plots of the crystallographic axes. Both samples are tested at the same stage rotation (SR) and stage tilt (ST). Full details of pillar geometry are in table 1. Images of the pillars before deformation can be found in Supplementary Materials (Figure A.1).

2017]. To date, micropillar experiments investigating geological materials have been scarce [Kranjc et al., 2020, Keller et al., 2017, Sly et al., 2020, Montagne et al., 2014, Korte and Clegg, 2009], and none have been conducted on isolated grain boundaries in geological materials. In this contribution, we bring these strategies together to test the relative shear strength of grain boundaries compared to crystal interiors at elevated temperatures.

2 Experimental methods

2.1 Sample preparation

We investigate two pure forsterite (Fo) bicrystal samples containing a low-angle grain boundary (LAGB, 4°, [100]/(014)) and a high-angle grain boundary (HAGB, 60°, [100]/(011)), respectively. The low-angle grain boundary is parallel to the (014) plane and the two crystals are misoriented around [100]. The high-angle grain boundary is parallel to the (011) plane, and the two crystals are misoriented around [100] [Marquardt and Faul, 2018, Adjaoud et al., 2012, Wagner et al., 2016]. The samples were prepared using the wafer-bonding technique [Heinemann et al., 2001, Hartmann et al., 2010]. This technique generates synthetic grain boundaries free of any induced plastic deformation and chemical contamination [Heinemann et al., 2001]. The grain-boundary misorientation angle is controlled in order to generate symmetric, low-energy, and near-coincidence grain boundaries [Heinemann et al., 2001, Hartmann et al., 2010, Marquardt and Faul, 2018, Adjaoud et al., 2012]. Similar samples to the HAGB bicrystal used in this study have been characterized in detail by Marquardt and Faul [2018], revealing that the high-angle grain-boundary width is less than 1 nm, and the plane includes segments that are faceted on the nm-scale [Figure 9, Marquardt and Faul, 2018]. For this HAGB structure, the

grain-boundary diffusivity coefficients have been calculated by Wagner et al. [2016], and the grain-boundary energy and the atomic structure have been calculated by Adjaoud et al. [2012] via molecular dynamics. The exactly same HAGB bicrystal sample has also been investigated via room-temperature nanoindentation by Avadanii et al. [2022]. In this paper, we use forsterite to refer to $\mathrm{Mg_2SiO_4}$ and olivine to refer exclusively to compositions including iron, which have been used in previous studies (e.g., San Carlos).

Figure 1 displays the bicrystal sample assembly for *in-situ* testing. We tilted the bicrystals in a steel mount and polished a surface at 45° to the grain-boundary plane. This new surface was perpendicular to the direction of subsequent micropillar compression such that shear-stresses were maximized on the grain boundary plane. Bicrystals were mounted with high-temperature Omegabond-600 cement. The surfaces were polished flat using diamond polycrystalline suspensions with grit sizes ranging from 9 μm down to 0.05 μm. The surfaces were finally polished with colloidal silica. The orientation of the bicrystals relative to the polished surface was determined using electron-backscatter diffraction (EBSD).

We tested micropillars containing the grain boundary as well as micropillars manufactured in the crystal interior (Figure 1, Table 1). Micropillars with nominal diameters of 2–2.5 μm and a height-to-diameter ratio of ∼1:3 were manufactured with a Zeiss-AURIGA Ga+ focused ion beam (FIB) using decreasingly smaller currents from 2 nA to 50 pA. The initial diameter, height, and tapering of the pillars were measured using scanning electron microscope (SEM) images and are reported in Table 1. Some micropillars were manufactured on the edge of the sample for optimal imagining conditions during pillar compression, as the TESCAN Mira3 SEM stage is tiled by 10° with respect to the SEM imagining angle (Figure 1). SEM images of the micropillars before deformation are presented in Supplementary Materials (Figure A.1).

2.2 Mechanical testing

The micropillars were compressed using a flat-end diamond tip (a 60° cone with a flat end) with a nominal diameter of 10 μm. We deformed the micropillars *in-situ* with a Hysitron PI88 SEM Picoindenter. The *in-situ* images were captured with a custom TESCAN Mira3 SEM. The mechanical tests were performed at 700°C with a load-controlled trapezoid function, with a maximum hold segment of 120 s (e.g., Figure A.6 in Supplementary Materials). Table 2 reports the time corresponding to constant load in each experiment. The loading rates for the LAGB and HAGB bicrystals were 2 mN/s and 0.8 mN/s, respectively. The micropillars within the bicrystal interior have trenches of 20 μm diameter milled around them, allowing the top 20% to be imaged during *in-situ* testing.

2.3 Calculations of stress and strain

Following the standard in high-temperature nanoindentation testing, corrections were made for thermal drift, machine compliance, and the point of zero displacement and load [e.g., Wheeler et al., 2015]. Measurements of the thermal drift were made over a time period of 40 s at the beginning of each test at a very low contact load (<20 μN). The average value measured in the final 20 s of the test was taken as an estimate of the average drift rate during the test and was used by the acquisition software to correct the measured displacements. In our tests, the total drift was on the order

of 10s of nm (Supplementary Materials, Figure A.2). The machine compliance was calibrated using bulk indents in the singe crystals away from the pillars, and the point of zero load and displacement was manually found for each test by inspecting the initial segment of the reported load-displacement curve. The identified point of zero load and displacement replaced the automated reported start of the test.

The experimental set-up in Figure 1 is influenced by the compliance of the instrument, the indenter tip, the steel and cement bond used in the sample assembly, and each pillar acting as a cylinder indenting into the substrate. Thus, we can describe the reported displacement, h_{rep}, as

$$h_{\mathrm{rep}} = h_{\mathrm{ms}} + h_{\mathrm{base}} + h_0 + h_{\mathrm{p}}, \tag{1}$$

where h_{ms} is the displacement due to the combined impact of the machine stiffness and the stiffness of the mounting assembly, h_{base} is the displacement due to the pillar base indenting into the bulk sample, h_0 is the difference between the reported point of first surface contact and the actual point of surface contact, and h_{p} is the displacement within the pillar of interest in response to an applied load. We accounted for h_0 by finding the point of surface contact at which displacement and load should be 0 after inspecting the reported load-displacement curves at small loads and noting a sharp increase in reported values.

The combined compliance of the machine and sample assembly was determined by using data collected from elastic experiments in the bulk sample. These experiments are indents at small loads placed in the crystal interior at 700°C, with no residual indent in the sample surface. Since there was no plastic penetration in the bulk sample surface, the contact area remained constant and the conical tip acted as a cylindrical punch. We compared these data to the calculated displacement, h, for an applied load, P, using Sneddon's solution for indenting with a flat-ended cylindrical punch into an elastic half space [Sneddon, 1965, Fischer-Cripps, 2011, Ch 3]

$$P = 2aE_{\mathrm{eff}}h, \tag{2}$$

where E_{eff} is the reduced modulus and a is the contact radius. We computed the reduced Young's modulus as $E_{\mathrm{eff}}^{-1} = \frac{1-vs^2}{Es} + \frac{1-vi^2}{Ei}$ using published values for the Poisson's ratio ($vs = 0.2465$) and Young's modulus ($Es = 180$ GPa) of forsterite at 700°C [Kumazawa and Anderson, 1969, Table 8] and $Ei = 1150$ GPa and $vi = 0.07$ for the conical indenter. The contact radius a has been estimated by measuring the imprint of the indenter into the sample surface in experiments conducted at higher loads, in which a small amount of plastic displacement (<100 nm) leads to an observable imprint. The measured diameter of the punch impression on SEM images is 5.6 μm.

We can calculate the error, h_{err}, due to the compliance of the system as the difference between the reported values, h_{rep}, and predicted values, h_{pred} using Equation 2. For each pillar, h_{ms} was calculated using the linear fit between h_{err} and P determined for each sample assembly (see Figure A.3 in Supplementary Materials).

The impact of the pillar indenting into the substrate, h_{base}, was computed by using Equation 2 and the measured values of the diameter at the bottom of the pillar displayed in Table 1. This correction is an approximation based on Sneddon's

solution for a perfect cylinder [Sneddon, 1965] and does not account for tapering or aspect ratio of the micropillar [Fei et al., 2012].

In order to calculate the stress-strain values using h_{p} determined from Equation 1 and reported values of the applied load, P, we explored two alternative sets of assumptions about the deformation style. In the first case, we assumed that the cross-sectional area of the pillar is constant. Here we assume that the applied load is purely uniaxial and centrosymmetric, the contact area between the flat punch and the deforming pillar stays nominally constant, and the contact area is equal to the area, A_0, at the top of the pillar such that the engineering stress, σ_{A}, is defined as

$$\sigma_{\mathrm{A}} = \frac{P}{A_0}, \tag{3}$$

and the engineering strain ε_{A}, is defined as

$$\varepsilon_{\mathrm{A}} = \frac{h_{\mathrm{p}}}{H_i}, \tag{4}$$

where H_i is the height of the pillar at the beginning of each test. Note that at the start of the first test, the height of the pillars is the height H_0, reported in Table 1. The height at the beginning of subsequent tests is H_0 minus the residual displacement, h_{r}, determined after unloading in the previous test. Therefore, $H_i = H_0 - h_{\mathrm{r}_{i-1}}$, where the value of the subscript i denotes the particular test, and n is the number of total tests of each pillar. The area A_0 at the top of the pillar was calculated using the diameter values reported in Table 1. Violating assumptions of constant area of contact through pillar tapering could result in a stress gradient with the highest stresses at the top of the pillar [Dehm et al., 2018].

In the second case, we assumed that the volume of the pillar was constant. Here, we assumed plastic deformation only, without any crack formation. We calculated the stress, σ_{V}, at constant volume as

$$\sigma_{\mathrm{V}} = \frac{P}{A_i} = \frac{PL_i}{V_0}, \tag{5}$$

where L_i is the length of the pillar during testing and is equal to the height H_i of the pillar at the start of each test minus the displacement h_{p} of the pillar, and V_0 is the initial volume. We calculate V_0 using the volume formula of a conical frustum

$$V_0 = \frac{\pi H_0}{3}\left[(r_{\mathrm{top}} + H_0\tan(\beta))^2 + 2r_{\mathrm{top}}^2 + r_{\mathrm{top}}H_0\tan(\beta)\right], \tag{6}$$

where β is the tapering angle measured using SEM images and reported in Table 1 and r_{top} is the radius at the top of the pillar. For samples with height to width ratios of 1:3 and taper angles of 2–3°, the resulting maximum errors in stress are 10–15% [Dehm et al., 2018]. We calculate the strain at constant volume ε_{V} using

$$\varepsilon_{\mathrm{V}} = \ln\frac{L_i}{H_{\mathrm{i}}}. \tag{7}$$

2.4 Microstructural investigations

We further characterized pillar 6 in the HAGB sample using scanning transmission electron microscopy (STEM) at Imperial College London. For these investigations, we coated the sample with a Pt layer and proceeded to prepare a

Table 1: Details of micropillars tested in this study, manufactured on a low-angle grain boundary (LAGB) bicrystal and a high-angle grain boundary (HAGB) bicrystal.

Sample	Pillar	Material	Height (μm)	Top diameter (μm)	Bottom diameter (μm)	Taper angle (°)
Fo014 LAGB	P5	bicrystal AB	7.2	2.12	3.41	3.9
	P6	crystal A	6.5	2.55	3.58	5.6
	P7	bicrystal AB	7.6	2.38	3.61	3.4
	P8	crystal B	7.2	2.49	3.40	2.9
Fo011 HAGB	P1	crystal A	7.2	2.89	3.60	2.6
	P2	crystal A	7.6	2.79	3.52	2.6
	P3	bicrystal BA	8.4	2.42	3.06	1.9
	P4	crystal B	9.0	2.55	3.67	3.2
	P5	bicrystal BA	8.0	2.42	3.08	2.0
	P6	bicrystal BA	8.0	2.42	3.05	1.8

TEM lamella that sectioned the pillar parallel to the compression direction. We used a standardised procedure to mill the TEM foil using a Ga^+ ion beam and to lift out the foil. We imaged the foil using STEM on a dual-beam Helios microscope operating at a voltage of 30 kV and emission current of 86 pA.

3 Results

3.1 Low-angle grain boundary bicrystal

The bicrystal containing the low-angle grain boundary (LAGB, Fo014) has been mounted such that the grain-boundary plane is at approximately 45° to the loading direction. The [100] axis is shared amongst the two crystals, while the [010] axis is perpendicular to the loading direction (see Figure 1a). The two crystals are misorieted around [100] by 4°. The loading direction of pillars in the crystals in the LAGB sample is close to the $[101]_c$ orientation in the convention of a cubic lattice [Durham and Goetze, 1977].

Figure 2 presents the reported load-displacement data for Fo014 grouped by the type of test. Pillars 5 and 6 (green outline) were tested at constant loading rate up to a load of 8 mN with no hold segment. Pillars 7 and 8 (brown outline) were tested at a constant loading rate up to loads of 4 and 5 mN, respectively, resulting in repeated tests with a hold segment of 60 s at the maximum load (Table 2, Figure A.6). In Figure 2, the pillar containing the grain boundary (P5) supports higher elastic loads than the pillar without the grain boundary. During the creep tests, P7 containing the grain boundary displays brittle failure after 500 nm of displacement, whereas P8 accommodates 2000 nm of displacement. Figure 3 displays further details of the correlation between the mechanical data and the *in-situ* observations. In P8, the significant drop in load during test 4 corresponds to slip band formation at an angle of 45° from the loading axis, towards the positive X_0 direction in the reference frame of the sample surface. Subsequent slip bands do not exhibit a corresponding load drop in the mechanical data.

Figures 4a and c display stress and strain assuming a constant contact area for the low-angle grain boundary, and Figures 4b and d display stress and strain for the same tests but assuming a constant volume. During the tests with a short load-hold segment, the pillar with the grain boundary (P5) yields at a stress of 0.6 GPa immediately followed by brittle

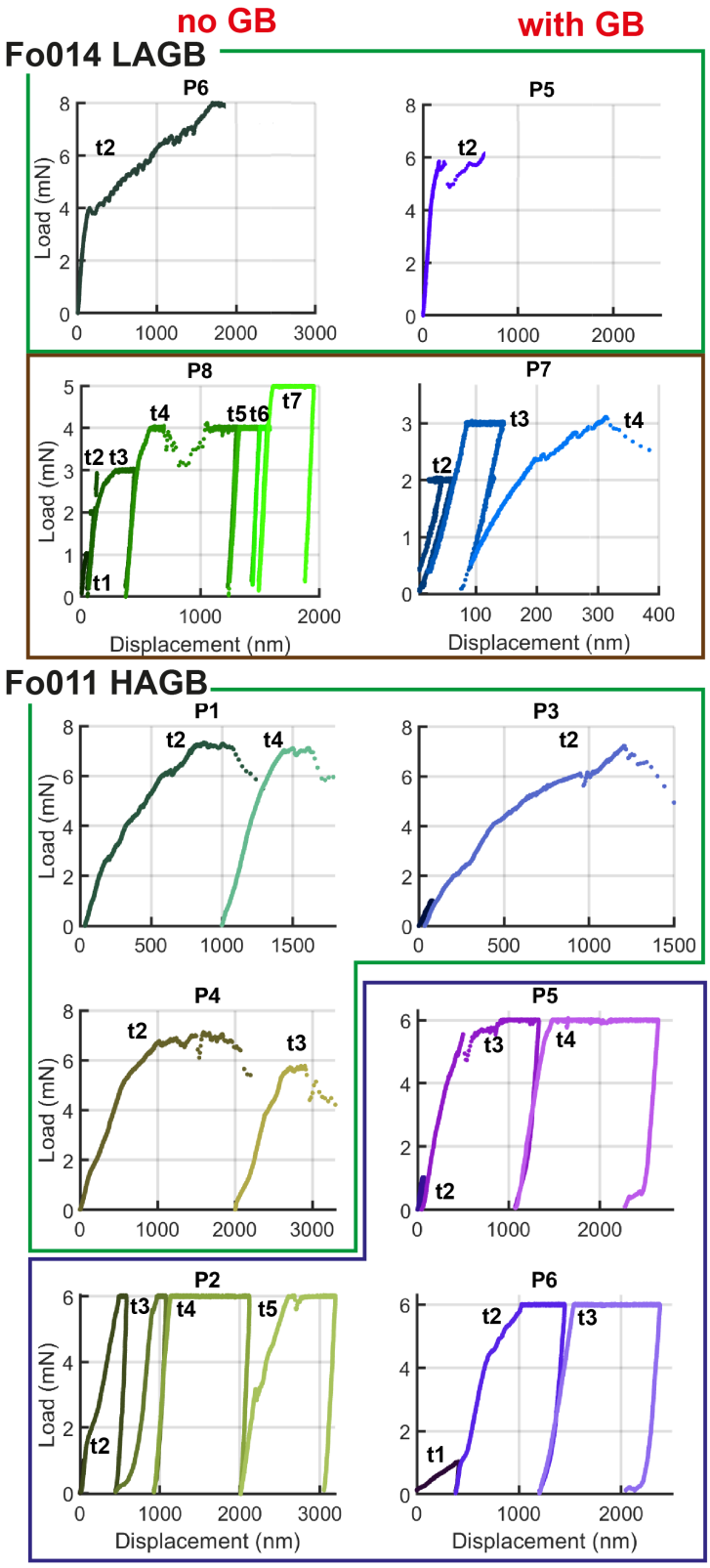

Figure 2: Load-displacement data for the micropillars described in Table 1. The left column corresponds to pillars in the single crystals, and the right column corresponds to pillars containing an interface. The outlined groups indicate tests conducted at similar maximum load and length of hold, as described in Table 2.

Table 2: Details of the mechanical tests on micropillars described in Table 1.

Sample	Pillar	Test	Max load (mN)	Load hold (s)	*In-situ* deformation observation
Fo014 LAGB	P5	1	1	10	system error
		2	8	60	permanent
	P6	1	1	10	system error
		2	8	60	permanent
	P7	1	1	10	system error
		2	2	10	elastic
		3	3	60	permanent
		4	4	60	permanent
	P8	1	1	60	elastic
		2	2	60	permanent
		3	3	60	permanent
		4	4	60	permanent
		5	4	60	permanent
		6	4	120	permanent
		7	5	60	permanent
Fo011 HAGB	P1	1	1	5	elastic
		2	8	5	permanent
		3	8	5	system error
		4	8	5	permanent
	P2	1	1	5	elastic
		2	6	10	permanent
		3	6	10	permanent
		4	6	60	permanent
		5	6	60	permanent
	P3	1	1	5	permanent
		2	8	5	permanent
	P4	1	1	5	elastic
		2	3	5	permanent
		3	3	5	permanent
	P5	1	1	5	permanent
		2	6	60	system error
		3	6	60	permanent
		4	6	60	permanent
	P6	1	1	5	permanent
		2	6	60	system error
		3	6	60	permanent

failure, while the pillar without the grain boundary (P6) yields at a stress of 0.3 GPa and sustains continued plastic deformation until eventual failure at about 0.6 GPa. During the creep tests in Figure 4c, the pillar without the grain boundary (P8) exhibits plasticity and sustains higher stresses for a significantly increased duration (see also Figure A.6a) compared to the pillar with the grain boundary (P7). Consequently, the computed stresses in Figure 4b and d have smaller values than the stresses calculated assuming a constant area of contact. Figure 6a documents in further detail the slip bands formed during test 4 in pillar 8 and during subsequent tests. We observe that the deformation in the pillar is localised in the slip band and the base of the pillar is relatively undeformed. Except pillar 8, all the pillars in the low-angle grain boundary bicrystal have been deformed to failure. Detailed SEM characterization can be found in Supplementary Materials (Figure A.4).

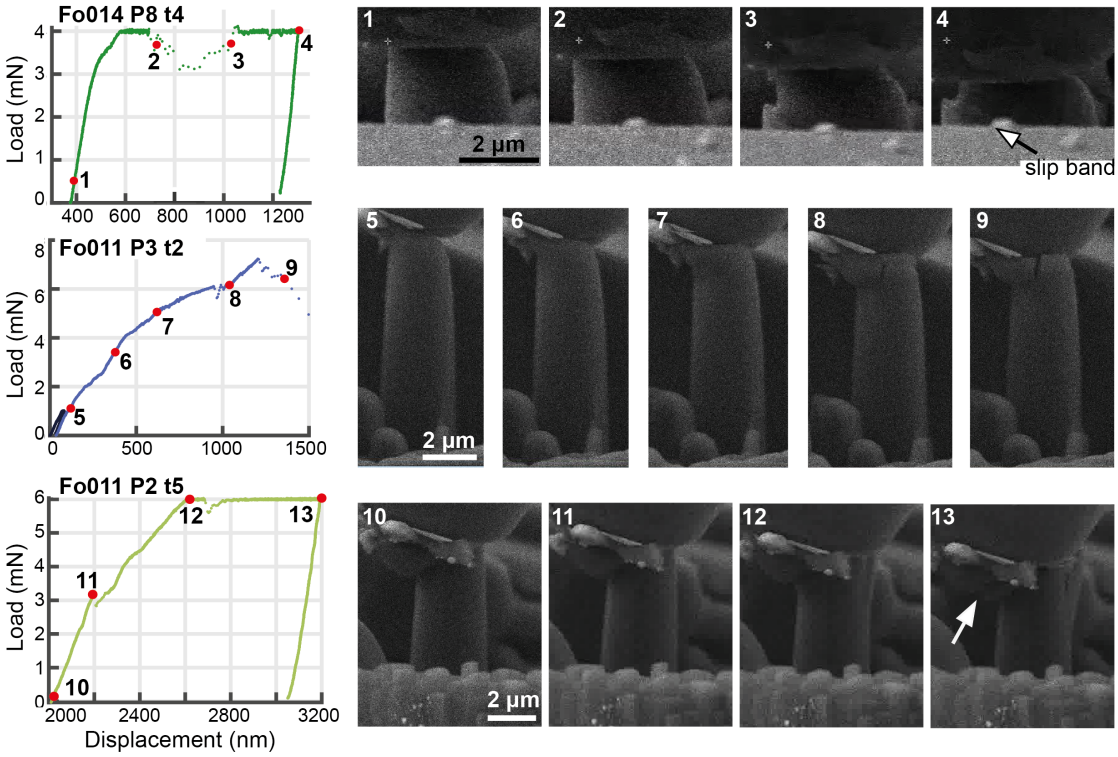

Figure 3: Examples of load-displacement curves alongside *in-situ* images. The white numbers on the images correspond to the marked red points in the load-displacement curves. The arrows mark slip bands.

3.2 High-angle grain boundary sample

The bicrystal containing the high-angle grain boundary (HAGB, Fo011) has been mounted such that the grain boundary plane is tilted 30° with respect to the loading direction. The [100] axis is shared amongst the two crystals, which is in the plane of the grain boundary. The two crystals are misoriented around [100] by 60°. In crystal $\mathrm{A_{HAGB}}$, the [010] axis is perpendicular to the loading direction, and the crystal orientation parallel to the loading direction is close to $[101]_c$ in the convention of a cubic lattice [Durham and Goetze, 1977]. In crystal $\mathrm{B_{HAGB}}$, the $[001]_c$ axis is close to perpendicular to the loading direction (Figure 1b).

Figure 2 presents the reported load-displacement data grouped by the type of test. Pillars 1, 3, 4 (in the green outline) were tested at constant loading rate up to a load of 8 mN with no hold segment (Table 2). The pillar containing the grain boundary (P3) underwent catastrophic failure after one test, whereas the pillars without the grain boundary (P1 and P4) sustained two cyclic tests up to 8 mN before catastrophic failure. Pillars 2, 5, 6 (purple outline) were tested with a load function with a hold segment of 60s at the maximum load of 6 mN, which is the approximate load of yielding for pillars 1, 3, 4.

Figure 3 presents the *in-situ* deformation of two pillars from the HAGB sample. Pillar 3 (P3) with the GB reaches catastrophic deformation at 6 mN. At this load, a crack initiates subparallel to the loading axis, before complete destruction at 7 mN. Pillar 2 (P2), without the GB, sustains multiple cycles of loading at 6 mN (Figure 2). After test 4,

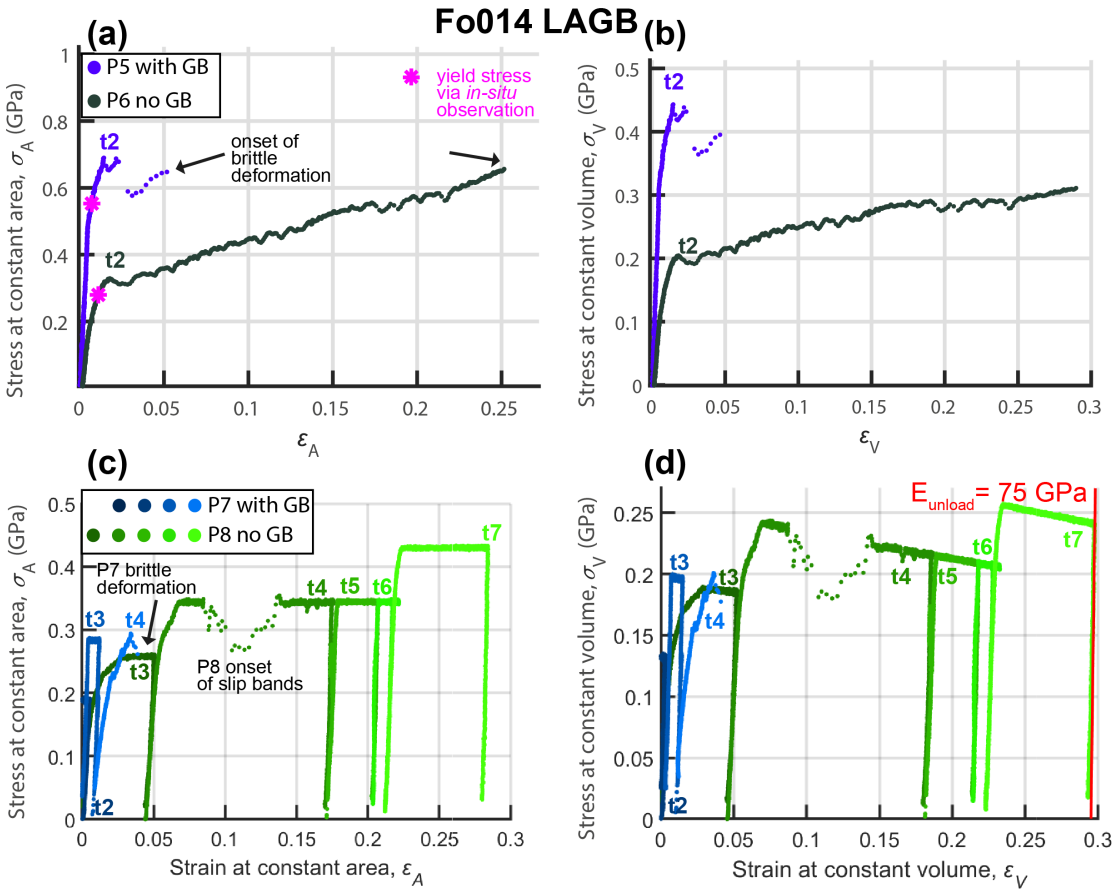

Figure 4: Compilation of stress-strain curves for the Fo014 sample with a low-angle grain boundary. Note the different scales of the vertical axes. a) Stress versus strain assuming a constant contact area during the experiment (Equations 4 and 3) for tests with a small holding segment at the maximum applied load (Table 2). The magenta stars mark the yield stress determined from *in-situ* observations. b) Stress versus strain assuming a constant volume of deformation during the experiment (Equations 7 and 5) for tests with a small holding segment at the maximum applied load (Table 2). c) Stress versus strain assuming a constant contact area during the experiment (Equations 4 and 3) for creep tests (Figure A.6). d) Stress versus strain assuming a constant volume of deformation during the experiment (Equations 7 and 5) for creep tests (Figure A.6).

the top part of pillar 2 forms slip bands developed at approximately 45° to the loading direction. Figure 3 displays further slip-band formation at the top of the pillar during test 5, as well as crack formation at the side of the pillar, parallel to the loading axis. No buckling or deformation is observed at the bottom of pillar 2 (see Supplementary Materials, Figure A.5).

Figures 5a and c display the stress-strain curves assuming a constant contact area for the high-angle grain boundary, and Figures 5b and d display the same stress and strain but assuming a constant volume. Pillars 1 (P1) and 4 (P4) without the grain boundary (Figure 5a) yield at a stress (assuming constant area) of 0.7 GPa and 0.75 GPa, respectively. The pillar containing the grain boundary, P3, yields at a stress of approximately 0.9 GPa. Figure 5a highlights that the pillars without the grain boundary accommodate more plastic strain prior to failure. Similar to the LAGB sample, assuming deformation at constant volume and using Equations 5 and 7 results in decreased values of stress and moderately increased values of strain (Figure 5b, d). Stress-strain curves for the creep tests are displayed in Figure 5c and d. The

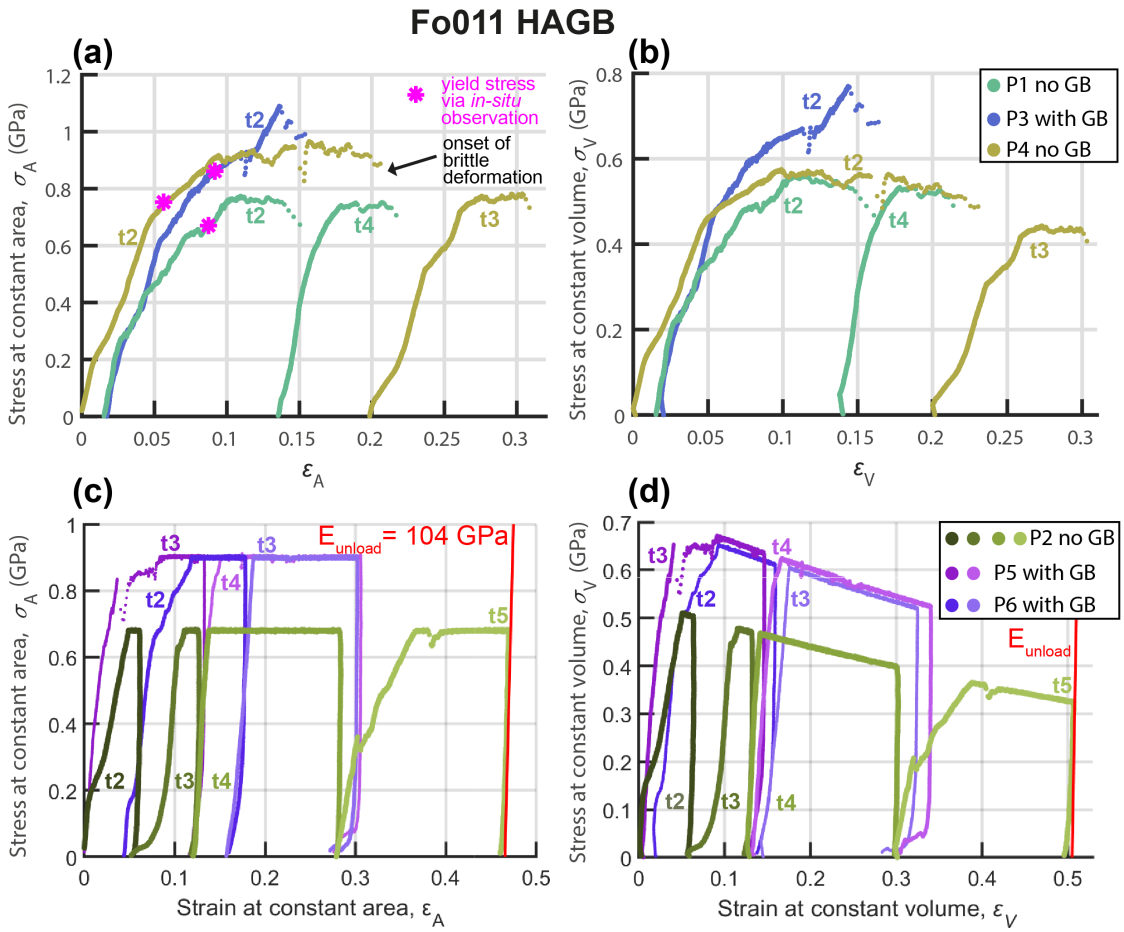

Figure 5: Compilation of stress-strain curves for the Fo011 sample with a high-angle grain boundary. Note the different scales of the vertical axes. a) Stress versus strain assuming a constant contact area during the experiment (Equations 4 and 3) for tests with a small holding segment at the maximum applied load (Table 2). The magenta stars mark the yield stress determined from *in-situ* observations. b) Stress versus strain assuming a constant volume of deformation during the experiment (Equations 7 and 5) for tests with a small holding segment at the maximum applied load (Table 2). c) Stress versus strain assuming a constant contact area during the experiment (Equations 4 and 3) for creep tests (Figure A.6). d) Stress versus strain assuming a constant volume of deformation during the experiment (Equations 7 and 5) for creep tests (Figure A.6).

pillars with the grain boundary, P5 and P6, deform at an imposed stress of approximately 0.9 GPa, while the pillar without the GB, P2, deforms at an imposed stress of 0.7 GPa. All the HAGB pillars in the creep tests accommodate a similar amount of plastic strain (Figure A.4b). This observation is also highlighted in strain-rate data in Figure A.6, Supplementary Materials.

Figure 6b displays post-deformation characterization of P5 and P6. Pillar 5 displays slip bands in both the $\mathrm{A}_{\mathrm{HAGB}}$ and $\mathrm{B}_{\mathrm{HAGB}}$ crystals, while P6 only has slip bands formed in the $\mathrm{B}_{\mathrm{HAGB}}$ crystal. The top crystal $\mathrm{B}_{\mathrm{HAGB}}$ in P5 and P6 has been sheared with a net displacement towards the $-X_0$ in the sample reference frame. The slip bands in the micropillars containing the bicrystal $\mathrm{BA}_{\mathrm{HAGB}}$ have a similar orientation to the ones in P2 in the single crystal $\mathrm{A}_{\mathrm{HAGB}}$ (Figure 3, Supplementary Materials Figure A.5). Notably, the slip bands observable in P5 and P6 are perpendicular to the GB plane, but do not intersect the GB. The interface is intact and does not display any evidence of sliding along

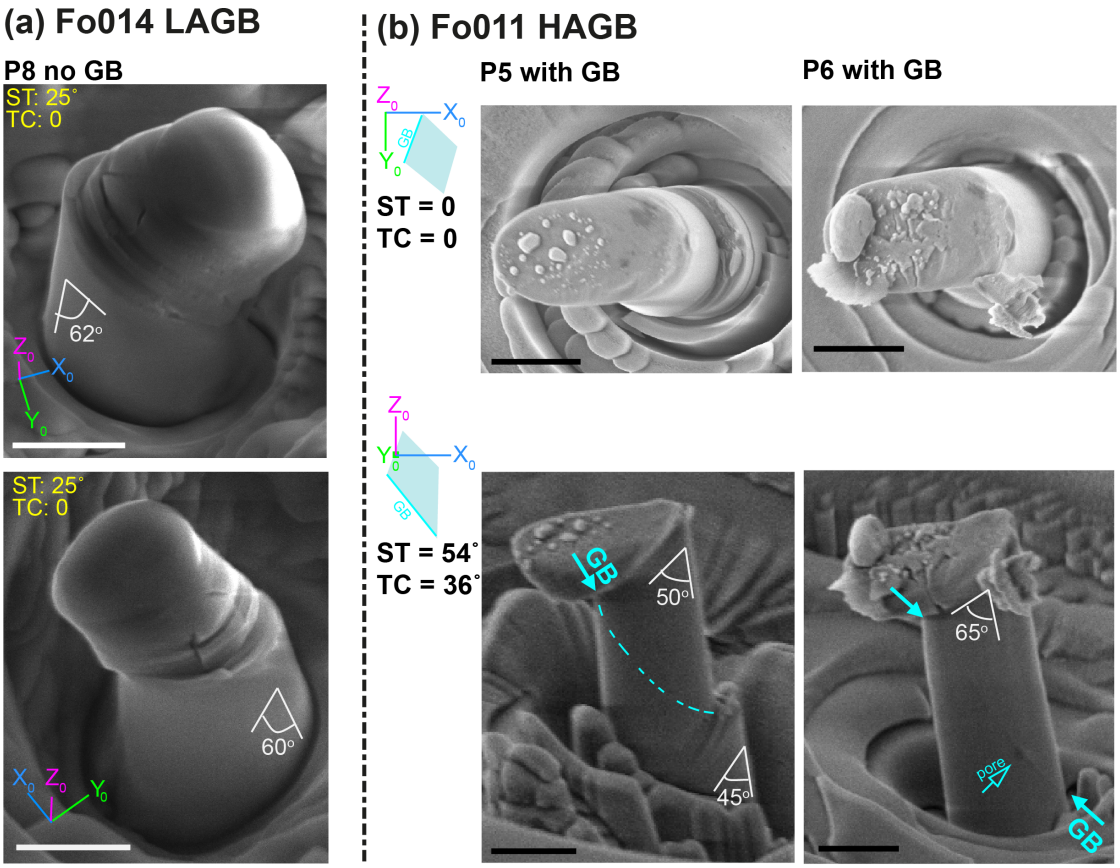

Figure 6: Compilation of images of deformed a) pillar 8 in the LAGB sample and b) pillars 5 and 6 containing the HAGB. The coordinate annotation references the coordinate system in Figure 1. All scalebars are 2 μm. Note that the images (and thus the angle) in panel a) have no tilt correction (TC) applied for the stage tilt (ST) of 25°. SEM characterization of all the pillars can be found in Supplementary Materials, Figures A.4 and A.5.

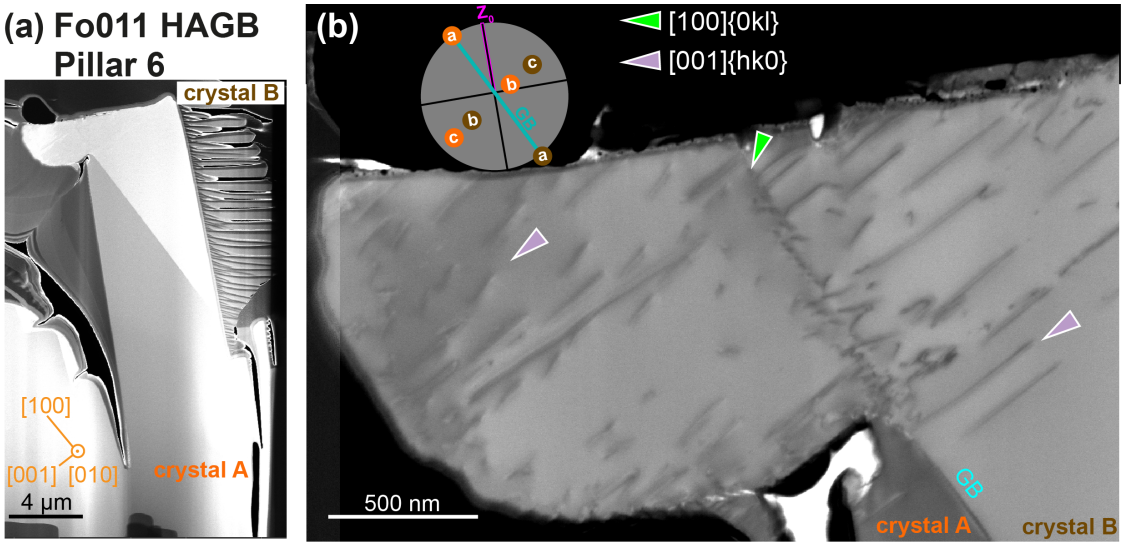

Figure 7: STEM images of a FIB lamella cut parallel to the indentation direction in pillar 6 in the HAGB sample. The lower hemisphere diagram is rotated such that the center of the diagram coincides with the axis perpendicular to the plane of view. a) Dark-field image of pillar 6 after deformation. b) Bright-field image of the upper part of deformed pillar 6.

the boundary (Figure 6b). In Figure 6b we observe a pore along the GB plane that was not imaged pre-deformation (Supplementary Materials Figure A.1). The pillars tested in this study accommodate plastic deformation mostly at the top of the pillar. This observation indicates that the stress calculations using the top diameter to estimate the contact area are reasonably representative of the stresses associated with deformation of the pillar (Figures 4a, c and 5a, c).

STEM characterization of P6 presented in Figure 7 reveals dislocation structures in the top crystal $\mathrm{B_{HAGB}}$, with dislocation lines appearing perpendicular to the GB plane. Figure 7a confirms that dislocation structures are present dominantly in crystal $\mathrm{B_{HAGB}}$, without any lattice distortion observable in the vicinity of the grain boundary. At higher magnifications in Figure 7b, we use the crystallographic orientation of dislocation lines to infer potential slip systems. The dislocations with lines in the plane of the section are consistent with [001] screw dislocations that could be operating as part of the [001]{hk0} slip system. Additionally, Figure 7b displays an array of dislocations colinear with the grain boundary with line directions perpendicular to the section (green arrow), which is consistent with the activity of edge dislocations on the [100]{0kl}) slip system. In Figure 7b, the grain boundary appears sheared along a direction perpendicular to the GB plane, which corresponds to the maximum resolved stresses in the pillar.

4 Discussion

In this study, we investigate the role of grain boundaries during deformation of forsterite at 700°C via *in-situ* micropillar compression, and we further characterize a deformed pillar using scanning transmission electron microscopy (STEM). Our key observations are that 1) grain boundaries do not accommodate any of the plastic strain, 2) pillars including a grain boundary display a slightly higher yield stress, and 3) pillars without a grain boundary display higher plastic strain before failure. We suggest that the presence or absence of a grain boundary is the primary factor leading to differences among pillars, rather than any differences in their geometry (see Table 1). As we outline below, we suggest that in our experiments, the grain boundaries lead to stress concentrations and strengthening.

4.1 General micropillar deformation

We observe that our micropillar experiments are characterized by an elastic loading regime, followed by yield at the top of the pillar, and sustained slip band formation and/or brittle deformation. In the LAGB (4°, [100]/(014)) sample, the geometry of deformation (Figure 6a) coupled with the crystallographic orientation (Figure 1a) indicate the occurrence of slip in the [001] direction on the (100) plane. Notably, only the first slip band generation in P8 is associated with a burst of displacement of $\sim$ 380 nm (Figure 3, frames 2–3, Figure A.4). We attribute this observation to a sudden activation of dislocations in a crystal with little initial dislocation sources [e.g., Dehm et al., 2018, Kumamoto et al., 2017]. We interpret plasticity during test 4 in P8, to be governed by dislocation nucleation, while in subsequent tests, plasticity is governed by dislocation motion. Similar stress drops in micropillar experiments have also been reported in sapphire [Montagne et al., 2014]. In the HAGB sample (60°, [100]/(011)), slip band formation is present in P2 in crystal $\mathrm{A_{HAGB}}$, in P5 in both crystals, and in P6 in the top crystal $\mathrm{B_{HAGB}}$ (Figures 1, 6, Table 1). Post-deformation

characterization of P2 (Supplementary Materials, Figure A.5) and the orientation of crystal $\mathrm{A_{HAGB}}$ (Figure 1b) suggest that the deformation is consistent with slip in the [001] direction on the (100) plane. In P5 and P6, the top crystal $\mathrm{B_{HAGB}}$ has been sheared in a direction corresponding to the [011] crystallographic axis. We suggest that this net deformation is generated by one or multiple slip systems in the [001] direction on {hk0} planes (Figure 7b), since there is no slip system with the [010] direction in forsterite [Demouchy, 2021].

The dominance of slip in the [001] direction is consistent with previous observations of olivine microstructures deformed in the low-temperature plasticity regime [e.g., Demouchy et al., 2013, Mussi et al., 2014, Raterron et al., 2004, Gaboriaud et al., 1981, Wallis et al., 2020]. Gaboriaud et al. [1981] use microstructures generated during high-temperature Vickers indentation tests on olivine single crystals to suggest that [001]{110} is activated at temperatures greater than 600°C, which is consistent with our experimental conditions. Wallis et al. [2020] present TEM data under a spherical indent in an olivine single crystal in a similar orientation with respect to the loading axis as crystal $\mathrm{B_{HAGB}}$ [sample OP4-2 in Kumamoto et al., 2017, Wallis et al., 2020]. The authors interpret the imaged dislocation structures as the activity of the [001](100) slip system split across multiple partial dislocations [Wallis et al., 2020]. Thus, we suggest that the main deformation regime in our experiments is low-temperature plasticity.

Previous studies of olivine rheology suggest that amorphization plays an important role at relatively low temperatures of deformation [Kranjc et al., 2020, Samae et al., 2021]. Kranjc et al. [2020] present microstructures documented after micropillar deformation at room temperature in a single crystal loaded parallel to the $[110]_{\mathrm{c}}$ orientation under a constant stress of ~ 4 GPa [Kranjc et al., 2020]. The authors interpret the resulting microstructures as amorphous shear bands parallel to (100), formed under a resolved shear stress of 2.2 GPa [Kranjc et al., 2020]. However, our documented dislocation structures (Figure 7) are consistent and share similarities with structures documented by Kranjc et al. [2020]. Thus, we are reinterpreting the data presented by Kranjc et al. [2020] as dislocations activated in the low-temperature plasticity regime. We suggest that the TEM observations presented by Kranjc et al. [2020] can be reconciled by the presence of slip systems with [001] on (100), (110) or (130) planes, observed dominantly in low-temperature deformation [Mussi et al., 2014]. Our suggestion is supported by the mechanical data presented by Kranjc et al. [2020], which agrees well with the low-temperature plasticity flow law calibrated by Kranjc et al. [2016]. Further spectral observations [Figure 5E in Kranjc et al., 2020] can be reconciled by structural damage induced by dislocations [for details, see Van Aken et al., 1998]. Furthermore, we suggest that the resolved shear stresses of 2.2 GPa in the experiments of Kranjc et al. [2020] are insufficient to promote amorphization of olivine, which has been documented at stresses higher than 30 GPa from shock experiments [Jeanloz et al., 1977] and anvil cell experiments [Lacam et al., 1980, Williams et al., 1990, Andrault et al., 1995].

4.2 The impact of grain boundaries on micropillar deformation

Experimental and theoretical studies highlight that grain boundaries influence deformation in olivine. Grain boundaries can enable grains to slide past each other. In these deformation regimes, the grain boundaries are relatively weak [e.g., dislocation-accommodated grain boundary sliding Hirth and Kohlstedt, 1995a, 2003, Hansen et al., 2011] and can

contribute to significant strain [e.g., diffusion creep Bollinger et al., 2019]. Grain boundaries can also represent barriers to the glide of lattice dislocations, leading to pile-ups. These arrays of dislocations generate long-range stresses within the crystal lattice, which further impact strain hardening and steady-state deformation at larger strains [e.g., Hansen et al., 2019, Wallis et al., 2020, Thom et al., 2022]. Gain boundaries can also represent a source [e.g., Avadanii et al., 2022] or a sink [e.g., Ferreira et al., 2021] for dislocations. These interactions underpin grain-size-sensitive deformation of olivine over a wide range of temperatures and grain sizes [Hansen et al., 2011, 2019, Kumamoto et al., 2017, Koizumi et al., 2020].

In these experiments, the grain boundary does not accommodate any of the observable plastic deformation. Permanent deformation is accommodated by slip bands perpendicular to the grain boundary plane (Figure 6). The two main groups of dislocations presented in Figure 7b are consistent with the activity of [001]{hk0} and [100]{0kl} slip systems, which have been previously documented in samples deformed in the low-temperature plasticity regime [e.g., Mussi et al., 2014, Wallis et al., 2020]. Figure 7b suggests that the shearing of crystal $\mathrm{B_{HAGB}}$ over crystal $\mathrm{A_{HAGB}}$ generates a complex stress state in which the bottom crystal $\mathrm{A_{HAGB}}$ acts as an indenter in the top crystal promoting dislocations parallel to the GB trace.

The resolved shear stresses are larger or similar on the interfaces compared to the theoretically available slip systems. These stresses further constrain the relative differences in strength between the single-crystal and bi-crystalline pillars. We use the stress values assuming constant area of contact (Figure 4c and 5c) and SEM images of pillars displaying slip band formation (Figures A.4 and A.5) to calculate the maximum imposed shear stress, τ, on the grain boundary and the observed slip bands using the Schmid law [Schmid and Boas, 1950]

$$\tau = \sigma_{\mathrm{A}} \cos(\phi) \cos(\lambda), \tag{8}$$

where ϕ is the angle between the normal to the plane and the applied force, and λ is the angle between the slip direction and the applied force. The term, $m = \cos(\phi)\cos(\lambda)$ represents the theoretical Schmid factor and ranges from 0 for the least favorably oriented slip plane to 0.5 for the most favorably oriented slip plane. Table 3 summarises these calculations. In the LAGB sample, the Schmid factor equals 0.5 for both the most favorable slip systems ([001](100) and [100](001)) and the GB plane. However, we only observe slip consistent with [001](100). This direct observation is consistent with previous experiments on olivine single crystals [Demouchy et al., 2013, Tielke et al., 2016a] and numerical models simulating [100] and [001] glide [Durinck et al., 2007] indicating that at low temperatures (<1000°C) and high stresses, the [001](100) slip system dominates deformation. In the HAGB sample, the Schmid factors are different for crystal $\mathrm{A_{HAGB}}$ (m=0.35 for [001](100)), and similar for the GB plane (m=0.43) and the top crystal $\mathrm{B_{HAGB}}$ (m = 0.43 for [001](100)). Even though the theoretical Schmid factors predict that the resolved shear stresses on the grain boundary are equal or higher than the shear stresses on the most favorably oriented slip system ([001](100)), we do not observe any sliding on the grain boundaries.

Table 3: Maximum imposed shear stresses during creep tests, τ, (Equation 8) on different planes in micropillars displaying slip band formation or containing an interface. The shear stresses calculated for pillars displaying slip band formation use Schmid factors computed using the angle between the slip trace and the edge of the pillar in Figures 6 and 7, and assuming a slip direction of [001].

Sample	Pillar	Material	Planar feature	τ (GPa)	Inferred active slip system
Fo014 LAGB	P8	crystal B	slip band	0.17	[001](100)
	P7	bicrystal AB	grain boundary	0.15	
Fo011 HAGB	P2	crystal A	slip band	0.29	[001](100)
	P5	crystal B	slip band	0.12	[001]{hk0}
	P5	crystal A	slip band	0.32	[001]{hk0}
	P5	bicrystal BA	grain boundary	0.39	
	P6	crystal B	slip band	0.13	[001]{hk0}
	P6	bicrystal BA	grain boundary	0.39	

The apparent lack of sliding on the interfaces in our experiments is consistent with predictions of grain-boundary viscosity following a model proposed by Ashby [1972], in which the high-angle grain boundary viscosity, η, is $\eta = \frac{kT}{8bD}$, where k is Boltzman's constant, D is the grain-boundary diffusion coefficient, and b is the length of the unit cell. In forsterite, $D = 10^{-28}\mathrm{m}^2/\mathrm{s}$ for $T = 700°\mathrm{C}$ and 1 atm [Fei et al., 2012, Wagner et al., 2016], and $b = 10.19 \times 10^{-10}$ m. Thus, $\eta = 16.5 \times 10^{15}\mathrm{Pa} \times \mathrm{s}$, which translates to a grain-boundary velocity of $4 \times 10^{-20}\mathrm{m/s}$ for an applied shear force of 0.4 N (e.g., P5 in the HAGB bicrystal), on a grain boundary with 1 nm thickness [Marquardt and Faul, 2018]. This calculation indicates that any grain-boundary sliding in these experimental conditions would be below the displacement measurement resolution of the apparatus. Based on predictions by Ashby [1972] we expect the low-angle GB to have an increased effective viscosity [Ashby, 1972].

Our experiments present evidence of grain boundaries acting as barriers to dislocation motion. STEM images indicate that the HAGB acts as a barrier to incoming dislocations (Figure 7). In Figure 8a, we compile the apparent yield stresses from Figures 4a and 5a for pillars containing the grain boundary (filled symbols) and pillars without the grain boundary (open symbols). Figure 8a indicates that within each bicrystal sample, the pillars containing the grain boundary (filled symbols) yield at higher stresses.

Care must be taken when comparing these different micromechanical data since deformation at these scales is often influenced by a well-documented size effect [e.g., Greer et al., 2005, Kraft et al., 2010, Korte-Kerzel, 2017, Kumamoto et al., 2017]. In Figure 8a we compare the yield stress in our pillar experiments (Figures 4a and 5a) to the yield stress calculated from hardness measurements at similar temperatures reported by Darot et al. [1985] in forsterite and Evans and Goetze [1979] in olivine single crystals. We transform published data of indentation with a Vickers pyramid to generate contact length and yield stress. In Vickers indentation, the maximum depth of contact is proportional to the diagonal of the imprint on the surface by a factor of 7 [Fischer-Cripps, 2011, Ch 2]. This proportionality is a direct result of the Vickers indenter geometry and allows us to transform diagonal lengths reported by Evans and Goetze [1979] and Darot et al. [1985] into indentation contact depth. We plot the reported yield stress by Evans and Goetze [1979] and use a similar constraint-factor approach to transform the hardness reported by Darot et al. [1985] into yield stress [Evans and Goetze, 1979]. We also note that previous indentation data indicate a higher yield stress compared to

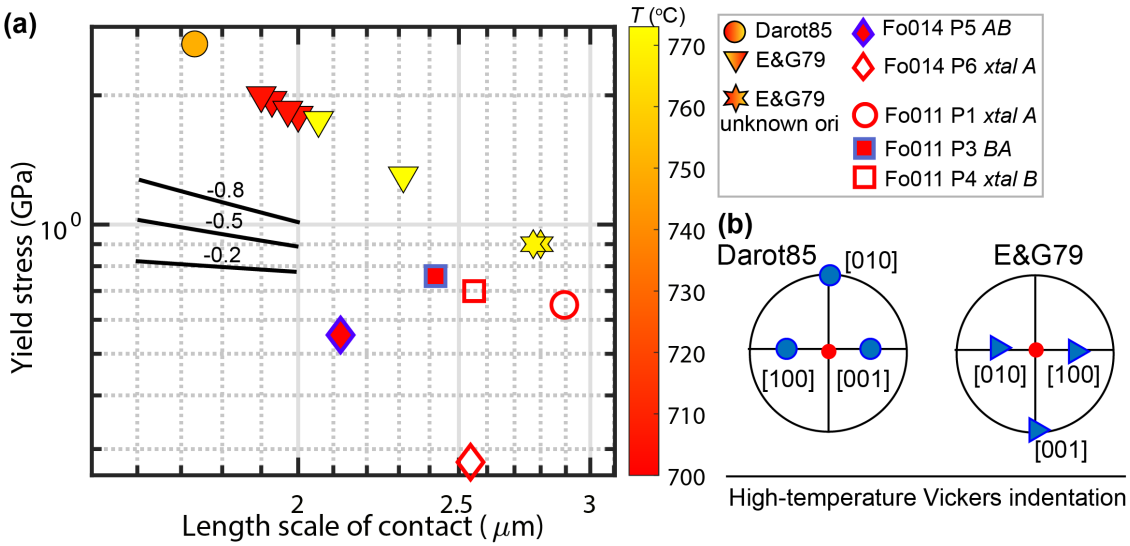

Figure 8: a) Yield stress from stress-strain curves in Figures 4a and 5a against Vickers indentation data from Darot et al. [1985] and Evans and Goetze [1979] on forsterite and olivine, respectively. All the included Vickers indents are at a maximum load of 0.5 N. b) Lower hemisphere plots describing the different orientations of the crystallographic axes with respect to the indentation direction.

our micropillar experiments. This discrepancy between indentation and micropillar strength has also been documented in calcite [Sly et al., 2020] and sapphire [Montagne et al., 2014] samples, and it is likely a result of differences in confining pressure in the two type of experiments. The size effect in the yield stress of olivine can account for some of the differences among bicrystalline and single crystal pillars, but do not fully explain the significant discrepancies among pillars in the LAGB sample (diamond symbols, Figure 8a). Thus, we suggest that the higher yield stress of the bicrystalline pillars is due to both a grain-size control and a slightly smaller length scale of contact. Observations of bicrystalline pillars having a higher yield stress than their single crystal counterparts have also been made in tests in which the grain boundary is parallel to the loading direction in pure Ta [Weaver et al., 2018], Ni [Kheradmand et al., 2013], and Cu [Imrich et al., 2014].

One consistent observation is that the onset of brittle deformation in the pillars with the GB is observed at smaller strains compared to the single crystal pillars (Figures 4 and 5). This observation suggests that elastic incompatibilities at the grain boundaries lead to locally elevated stresses that exceed the fracture toughness of the material. We note that, given sufficient confining pressure, these local stresses could lead to dislocation nucleation rather than fracture. This hypothesis is consistent with observations presented by Avadanii et al. [2022], who suggest that this HAGB sample promoted dislocation nucleation underneath spherical indents at indentation shear stresses up to 10 GPa [see their Supplementary Materials, Avadanii et al., 2022].

5 Implications

In-situ micropillar experiments on pure forsterite grain boundaries at 700°C reveal that pillars containing the grain boundary consistently support higher elastic loads compared to the pillars in the single crystal. Additionally, the pillars in the single crystal sustain higher plastic strain compared to the bicrystalline pillars. The grain boundary has been oriented at $\sim 45^{\circ}$ to the loading direction. Under these experimental conditions no sliding associated with the grain boundary has been recorded.

Observations presented in this study support the hypothesis that in forsterite, the most energetically favorable grain boundaries [Marquardt et al., 2015] are relatively stronger compared to the available slip systems for deformation at high stresses. This hypothesis underpins observations of grain-size effects of the bulk yield stress in olivine low-temperature plasticity [Hansen et al., 2019]. However, as grain-boundary diffusion rates increase with temperature [Fei et al., 2016, Wagner et al., 2016] we expect a decrease in grain-boundary viscosity [Ashby, 1972] and an increase in grain-boundary mediated deformation (e.g., GBS, Hansen et al. [2011]). In a deforming polycrystalline material, the relative strength of the GBs at the same temperature varies with grain boundary character and orientation according to predictions by Ashby [1972]. Therefore, with increasing deformation, the distribution of GBs might influence the bulk patterns of plastic anisotropy, and consequently, strain localization.

We have also demonstrated that miniaturised mechanical testing facilitates measurements of isolated microstructural features in olivine. Experimental studies on olivine single crystals using a confining pressure document a transition between the dominance of [001](100) slip system [Raleigh, 1968, Demouchy et al., 2013, Tielke et al., 2016a] at temperatures smaller than 1000°C, after which [100](001) is also activated [Raleigh, 1968, Durinck et al., 2007, Demouchy et al., 2013, Tielke et al., 2016a]. Experiments also document a change in relative strengths of [100](010) and [001](010) slip systems with confining pressure [Raterron et al., 2007]. Therefore, future micropillar experiments at the higher-end of technical capabilities and increased miniaturisation [e.g., Idrissi et al., 2016] might provide a detailed, quantifiable, and *in-situ* understanding of the relative strengths of slip systems in olivine.

6 Acknowledgments

DA is grateful to the UK National Environmental Research Council, and the Oxford Doctoral Training Partnership for DPhil studentship and funding [grant number NE/L002612/1]. LH, KM, DA, and AW acknowledge funding from UK National Environmental Research Council, via the NERC Standard Grant [grant number NE/S00162X/1]. LH acknowledges funding from the National Science Foundation [grant number NSF-EAR Grant 2022433].

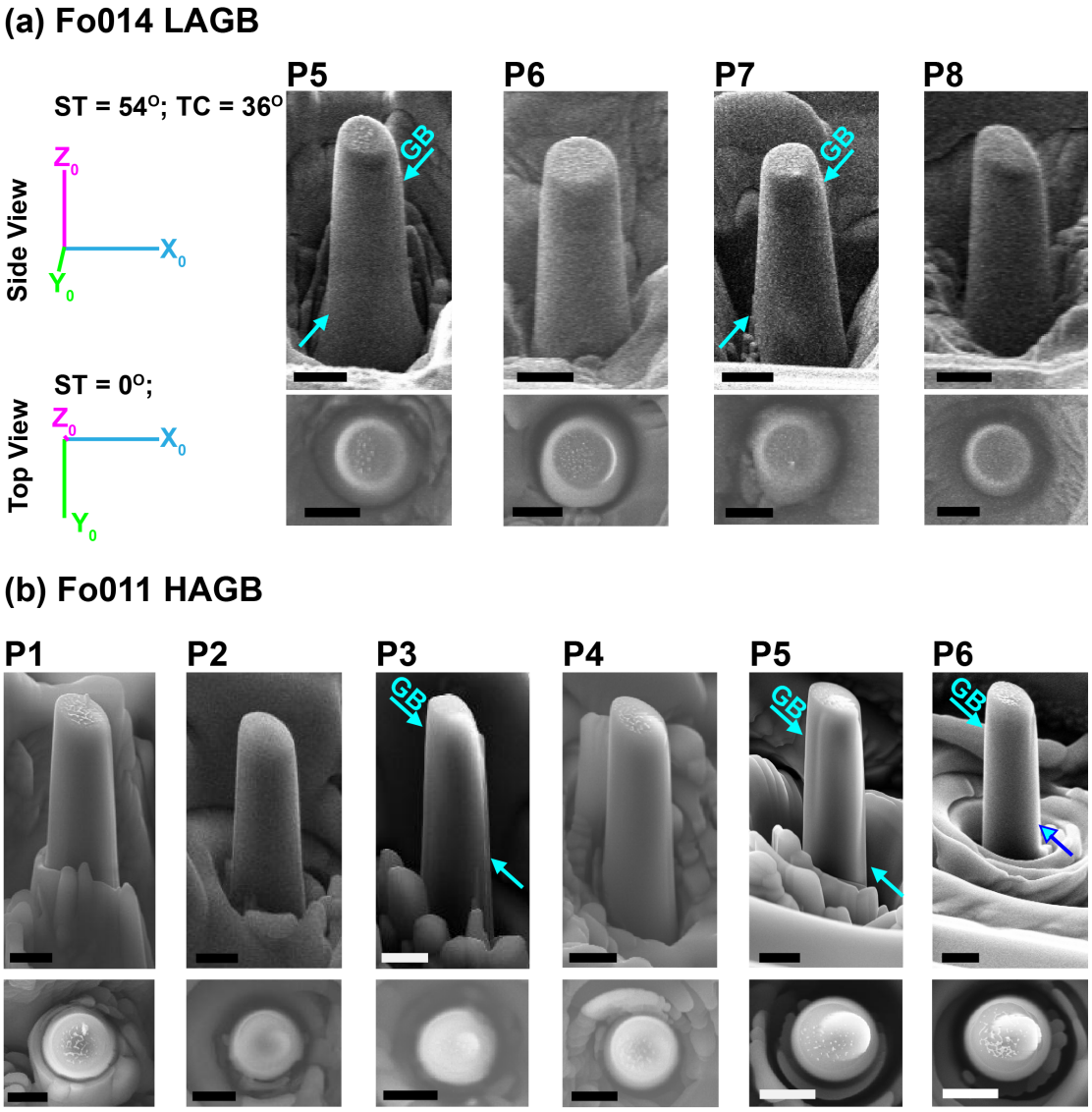

Figure A.1: SEM images of the micropillars in this study before deformation. The first row represent the side view imaged at stage stilt (ST) of 54°, with a tilt correction (TC) of 36°. The second row in each subfigure represents the top view of the micropillars. The axis represent the coordinate system in the reference plane of the sample surface and remain consistent within each row. The blue arrows mark the trace of the grain boundary. a) Micropillars containing a low-angle grain boundary. b) Micropillars containing the high-angle grain boundary. All scalebars are 2 μm.

A Supplementary Materials

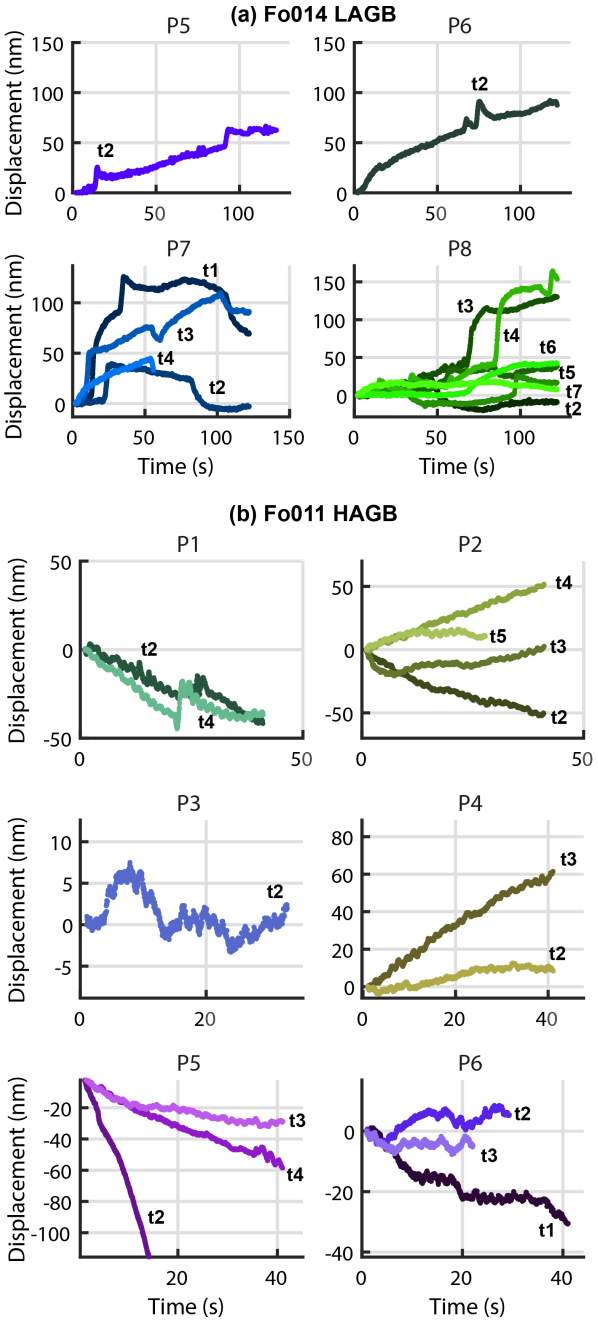

Figure A.2: Thermal drift of displacements during tests in the a) low-angle grain boundary sample and b) high-angle grain boundary sample. These drifts have been automatically accounted for by the acquisition software.

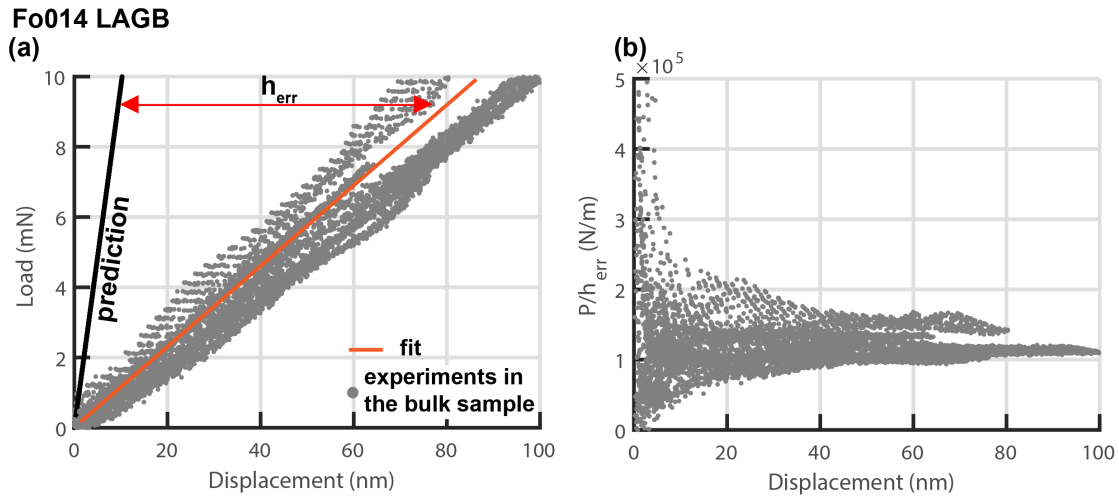

Figure A.3: Example of experiments used for correcting the impact of the compliance of the machine and the sample assembly. a) The prediction is calculated using Equation 2 and compared with experiments in the bulk crystal at 700°C (grey) to calculate the error. b) The reported load divided by the computed error is proportional to the compliance of the system.

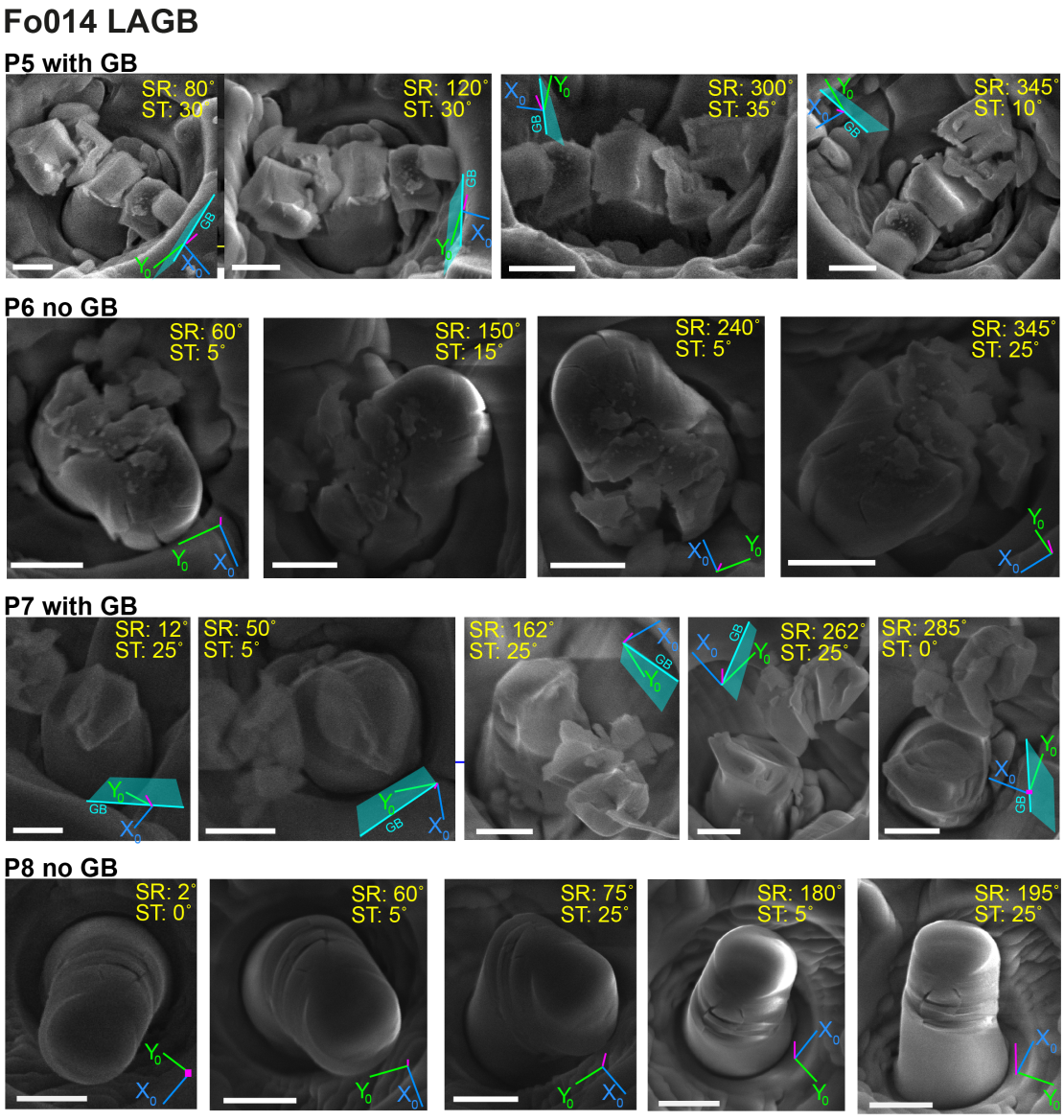

Figure A.4: Post-deformation SEM characterization of micropillars in the LAGB sample Fo014. The color-coded axis track the rotation of the surface rotation with respect to Figure 1 a). Stage rotation (SR) and stage tilt (ST) denote the stage position during image acquisition. The tilt correction is 0 in all images. The scalebars are 2 μm. The fracture in P7 is consistent with cleavage on the (010) plane.

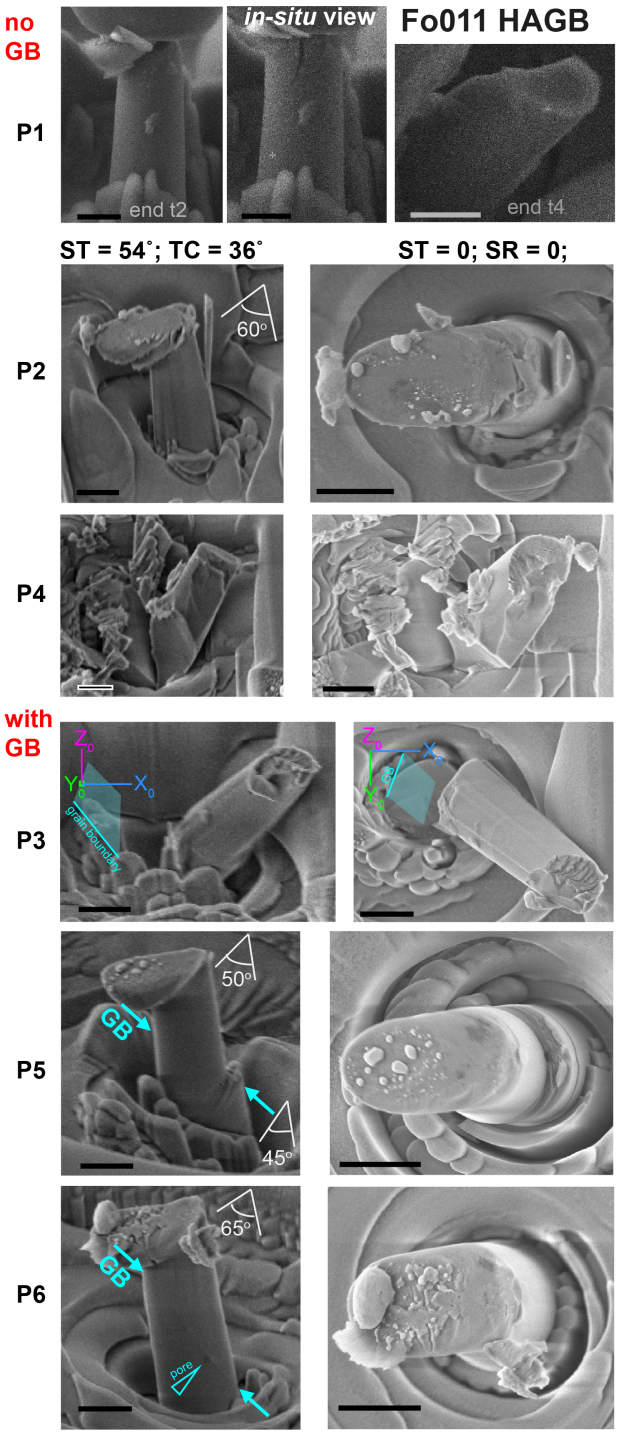

Figure A.5: Post-deformation SEM characterization of micropillars in the HAGB sample Fo011. The color-coded axis track the rotation of the surface rotation with respect to Figure 1 b). The top row displays images during the deformation experiments for P1, which has been decoupled from the base and lost during the indenter lift. Vertical fracture in P4, P3, and possibly P1 correspond to fracture along the (010) plane, which is the cleavage plane of forsterite [Durham et al., 1979, Darot et al., 1985]. For the remaining pillars, the first column is the side view, and the second column is the top view. Stage tilt (ST) and tilt correction (TC) denote image acquisition settings. The scalebars are 2 μm.

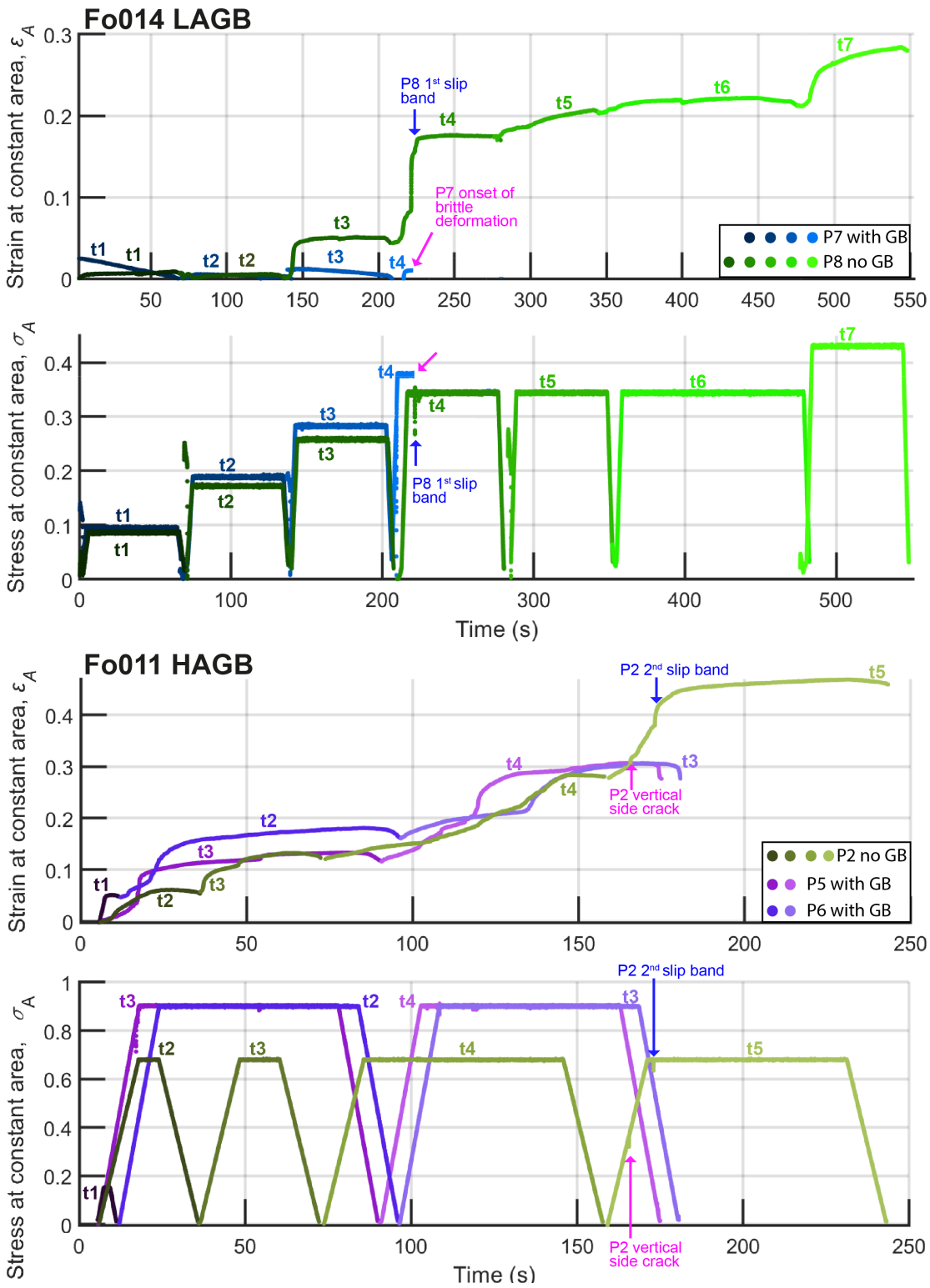

Figure A.6: Strain versus time in the creep tests detailed in Table 2.

References

Greg Hirth and D Kohlstedt. Rheology of the upper mantle and the mantle wedge: A view from the experimentalists. *Geophysical monograph-american geophysical union*, 138:83–106, 2003.

J Hunter and AB Watts. Gravity anomalies, flexure and mantle rheology seaward of circum-pacific trenches. *Geophysical Journal International*, 207(1):288–316, 2016.

Shijie Zhong and AB Watts. Lithospheric deformation induced by loading of the hawaiian islands and its implications for mantle rheology. *Journal of Geophysical Research: Solid Earth*, 118(11):6025–6048, 2013.

Lars N Hansen, Kathryn M Kumamoto, Christopher A Thom, David Wallis, William B Durham, David L Goldsby, Thomas Breithaupt, Cameron D Meyers, and David L Kohlstedt. Low-temperature plasticity in olivine: Grain size, strain hardening, and the strength of the lithosphere. *Journal of Geophysical Research: Solid Earth*, 124(6): 5427–5449, 2019.

Shun-ichiro Karato. Rheology of the earth's mantle: A historical review. *Gondwana Research*, 18(1):17–45, 2010.

LN Hansen and David L Kohlstedt. 2.18 constitutive equations, rheological behavior, and viscosity of rocks. *Treatise on Geophysics, second edition*, 2:441–472, 2015.

Manuel Thieme, Sylvie Demouchy, David Mainprice, Fabrice Barou, and Patrick Cordier. Stress evolution and associated microstructure during transient creep of olivine at 1000–1200 c. *Physics of the Earth and Planetary Interiors*, 278:34–46, 2018.

Caroline Bollinger, Katharina Marquardt, and Filippe Ferreira. Intragranular plasticity vs. grain boundary sliding (gbs) in forsterite: Microstructural evidence at high pressures (3.5–5.0 gpa). *American Mineralogist: Journal of Earth and Planetary Materials*, 104(2):220–231, 2019.

Ulrich H Faul, JD Fitz Gerald, RJM Farla, Rose Ahlefeldt, and Ian Jackson. Dislocation creep of fine-grained olivine. *Journal of Geophysical Research: Solid Earth*, 116(B1), 2011.

Lars N Hansen, Mark E Zimmerman, Amanda M Dillman, and David L Kohlstedt. Strain localization in olivine aggregates at high temperature: A laboratory comparison of constant-strain-rate and constant-stress boundary conditions. *Earth and Planetary Science Letters*, 333:134–145, 2012a.

Jacob A Tielke, Mark E Zimmerman, and David L Kohlstedt. Direct shear of olivine single crystals. *Earth and Planetary Science Letters*, 455:140–148, 2016a.

J Kacher, C Kirchlechner, J Michler, E Polatidis, R Schwaiger, H Van Swygenhoven, M Taheri, and Marc Legros. Impact of in situ nanomechanics on physical metallurgy. *Mrs Bulletin*, 44(6):465–470, 2019.

Harold J Frost and Michael F Ashby. *Deformation mechanism maps: the plasticity and creep of metals and ceramics*. Pergamon press, 1982.

Kelly Kranjc, Zachary Rouse, Katharine M Flores, and Philip Skemer. Low-temperature plastic rheology of olivine determined by nanoindentation. *Geophysical Research Letters*, 43(1):176–184, 2016.

Sylvie Demouchy, Andréa Tommasi, Tiziana Boffa Ballaran, and Patrick Cordier. Low strength of earth's uppermost mantle inferred from tri-axial deformation experiments on dry olivine crystals. *Physics of the Earth and Planetary Interiors*, 220:37–49, 2013.

Brian Evans and Christopher Goetze. The temperature variation of hardness of olivine and its implication for polycrystalline yield stress. *Journal of Geophysical Research: Solid Earth*, 84(B10):5505–5524, 1979.

Hosni Idrissi, Caroline Bollinger, Francesca Boioli, Dominique Schryvers, and Patrick Cordier. Low-temperature plasticity of olivine revisited with in situ tem nanomechanical testing. *Science advances*, 2(3):e1501671, 2016.

Anthony Druiventak, Claudia A Trepmann, Jörg Renner, and Karin Hanke. Low-temperature plasticity of olivine during high stress deformation of peridotite at lithospheric conditions—an experimental study. *Earth and Planetary Science Letters*, 311(3-4):199–211, 2011.

S Mei, AM Suzuki, DL Kohlstedt, NA Dixon, and WB Durham. Experimental constraints on the strength of the lithospheric mantle. *Journal of Geophysical Research: Solid Earth*, 115(B8), 2010.

Paul Raterron, Yujun Wu, Donald J Weidner, and Jiuhua Chen. Low-temperature olivine rheology at high pressure. *Physics of the Earth and Planetary Interiors*, 145(1-4):149–159, 2004.

Kathryn M Kumamoto, Christopher A Thom, David Wallis, Lars N Hansen, David EJ Armstrong, Jessica M Warren, David L Goldsby, and Angus J Wilkinson. Size effects resolve discrepancies in 40 years of work on low-temperature plasticity in olivine. *Science advances*, 3(9):e1701338, 2017.

Sanae Koizumi, Takehiko Hiraga, and Tohru S Suzuki. Vickers indentation tests on olivine: size effects. *Physics and Chemistry of Minerals*, 47(2):1–14, 2020.

EO Hall. The deformation and ageing of mild steel: Iii discussion of results. *Proceedings of the Physical Society. Section B*, 64(9):747, 1951.

NJ Petch. The cleavage strength of polycrystals. *Journal of the iron and steel institute*, 174:25–28, 1953.

Zachary C Cordero, Braden E Knight, and Christopher A Schuh. Six decades of the hall–petch effect–a survey of grain-size strengthening studies on pure metals. *International Materials Reviews*, 61(8):495–512, 2016.

David Wallis, Lars N Hansen, Kathryn M Kumamoto, Christopher A Thom, Oliver Plümper, Markus Ohl, William B Durham, David L Goldsby, David EJ Armstrong, Cameron D Meyers, et al. Dislocation interactions during low-temperature plasticity of olivine and their impact on the evolution of lithospheric strength. *Earth and Planetary Science Letters*, 543:116349, 2020.

MF Ashby. Boundary defects, and atomistic aspects of boundary sliding and diffusional creep. *Surface Science*, 31: 498–542, 1972.

Rishi Raj and MF Ashby. On grain boundary sliding and diffusional creep. *Metallurgical transactions*, 2(4):1113–1127, 1971.

R Raj and MF Ashby. Grain boundary sliding, and the effects of particles on its rate. *Metallurgical and Materials Transactions B*, 3(7):1937–1942, 1972.

Terence G Langdon. Seventy-five years of superplasticity: historic developments and new opportunities. *Journal of materials science*, 44:5998–6010, 2009.

Greg Hirth and David L Kohlstedt. Experimental constraints on the dynamics of the partially molten upper mantle: 2. deformation in the dislocation creep regime. *Journal of Geophysical Research: Solid Earth*, 100(B8):15441–15449, 1995a.

Greg Hirth and David L Kohlstedt. Experimental constraints on the dynamics of the partially molten upper mantle: Deformation in the diffusion creep regime. *Journal of Geophysical Research: Solid Earth*, 100(B2):1981–2001, 1995b.

LN Hansen, ME Zimmerman, and David L Kohlstedt. Grain boundary sliding in san carlos olivine: Flow law parameters and crystallographic-preferred orientation. *Journal of Geophysical Research: Solid Earth*, 116(B8), 2011.

Jacob A Tielke, Lars N Hansen, Miki Tasaka, Cameron Meyers, Mark E Zimmerman, and David L Kohlstedt. Observations of grain size sensitive power law creep of olivine aggregates over a large range of lattice-preferred orientation strength. *Journal of Geophysical Research: Solid Earth*, 121(2):506–516, 2016b.

K Yabe, K Sueyoshi, and T Hiraga. Grain-boundary diffusion creep of olivine: 1. experiments at 1 atm. *Journal of Geophysical Research: Solid Earth*, 125(8):e2020JB019415, 2020.

N Kim, A Ando, K Yabe, and T Hiraga. Olivine morphology and fabric during diffusion creep: Pure shear experiments. *Journal of Geophysical Research: Solid Earth*, 127(5):e2021JB023613, 2022.

Ian Jackson, Ulrich H Faul, and Richard Skelton. Elastically accommodated grain-boundary sliding: New insights from experiment and modeling. *Physics of the Earth and Planetary Interiors*, 228:203–210, 2014.

LN Hansen, ME Zimmerman, and DL Kohlstedt. The influence of microstructure on deformation of olivine in the grain-boundary sliding regime. *Journal of Geophysical Research: Solid Earth*, 117(B9), 2012b.

Tomohiro Ohuchi, Takaaki Kawazoe, Yuji Higo, Ken-ichi Funakoshi, Akio Suzuki, Takumi Kikegawa, and Tetsuo Irifune. Dislocation-accommodated grain boundary sliding as the major deformation mechanism of olivine in the earth's upper mantle. *Science advances*, 1(9):e1500360, 2015.

Ulrich Faul and Ian Jackson. Transient creep and strain energy dissipation: An experimental perspective. *Annual Review of Earth and Planetary Sciences*, 43:541–569, 2015.

Vahid Samae, Patrick Cordier, Sylvie Demouchy, Caroline Bollinger, Julien Gasc, Sanae Koizumi, Alexandre Mussi, Dominique Schryvers, and Hosni Idrissi. Stress-induced amorphization triggers deformation in the lithospheric mantle. *Nature*, 591(7848):82–86, 2021.

Xiao-Yu Sun, Patrick Cordier, Vincent Taupin, Claude Fressengeas, and Sandro Jahn. Continuous description of a grain boundary in forsterite from atomic scale simulations: the role of disclinations. *Philosophical Magazine*, 96(17): 1757–1772, 2016.

Patrick Cordier, Sylvie Demouchy, Benoit Beausir, Vincent Taupin, Fabrice Barou, and Claude Fressengeas. Disclinations provide the missing mechanism for deforming olivine-rich rocks in the mantle. *Nature*, 507(7490):51–56, 2014.

Julien Gasc, Sylvie Demouchy, Fabrice Barou, Sanae Koizumi, and Patrick Cordier. Creep mechanisms in the lithospheric mantle inferred from deformation of iron-free forsterite aggregates at 900–1200° c. *Tectonophysics*, 761: 16–30, 2019.

Filippe Ferreira, Lars N Hansen, and Katharina Marquardt. The effect of grain boundaries on plastic deformation of olivine. *Journal of Geophysical Research: Solid Earth*, 126(7):e2020JB020273, 2021.

Katharina Marquardt and Ulrich H Faul. The structure and composition of olivine grain boundaries: 40 years of studies, status and current developments. *Physics and Chemistry of Minerals*, 45(2):139–172, 2018.

Sylvie Demouchy. Defects in olivine. *European Journal of Mineralogy*, 33(3):249–282, 2021.

Gerhard Dehm, Balila Nagamani Jaya, Rejin Raghavan, and Christoph Kirchlechner. Overview on micro-and nanomechanical testing: New insights in interface plasticity and fracture at small length scales. *Acta Materialia*, 142: 248–282, 2018.

Joana Polednia, Ralf Dohmen, and Katharina Marquardt. Grain boundary diffusion and its relation to segregation of multiple elements in yttrium aluminum garnet. *European Journal of Mineralogy*, 32(6):675–696, 2020.

Katharina Marquardt, Quentin M Ramasse, Christian Kisielowski, and Richard Wirth. Diffusion in yttrium aluminium garnet at the nanometer-scale: Insight into the effective grain boundary width. *American Mineralogist*, 96(10): 1521–1529, 2011.

Emmanuel Gardés, David Gibouin, Bertrand Radiguet, Adrian David, Wilfrid Prellier, and Katharina Marquardt. Magnesium transport in olivine mantle: new insights from miniaturized study of volume and grain boundary diffusion in mg2sio4 bi-crystals. *Contributions to Mineralogy and Petrology*, 176(12):1–16, 2021.

Sandra Korte-Kerzel. Microcompression of brittle and anisotropic crystals: recent advances and current challenges in studying plasticity in hard materials. *Mrs Communications*, 7(2):109–120, 2017.

Kelly Kranjc, Arashdeep S Thind, Albina Y Borisevich, Rohan Mishra, Katharine M Flores, and Philip Skemer. Amorphization and plasticity of olivine during low-temperature micropillar deformation experiments. *Journal of Geophysical Research: Solid Earth*, 125(5):e2019JB019242, 2020.

Lukas M Keller, Jakob J Schwiedrzik, Philippe Gasser, and Johann Michler. Understanding anisotropic mechanical properties of shales at different length scales: In situ micropillar compression combined with finite element calculations. *Journal of Geophysical Research: Solid Earth*, 122(8):5945–5955, 2017.

Michael K Sly, Arashdeep S Thind, Rohan Mishra, Katharine M Flores, and Philip Skemer. Low-temperature rheology of calcite. *Geophysical Journal International*, 221(1):129–141, 2020.

Alex Montagne, Siddhartha Pathak, Xavier Maeder, and Johann Michler. Plasticity and fracture of sapphire at room temperature: Load-controlled microcompression of four different orientations. *Ceramics International*, 40(1): 2083–2090, 2014.

S Korte and WJ Clegg. Micropillar compression of ceramics at elevated temperatures. *Scripta Materialia*, 60(9): 807–810, 2009.

Omar Adjaoud, Katharina Marquardt, and Sandro Jahn. Atomic structures and energies of grain boundaries in mg2sio4 forsterite from atomistic modeling. *Physics and Chemistry of Minerals*, 39(9):749–760, 2012.

Johannes Wagner, Omar Adjaoud, Katharina Marquardt, and Sandro Jahn. Anisotropy of self-diffusion in forsterite grain boundaries derived from molecular dynamics simulations. *Contributions to Mineralogy and Petrology*, 171(12): 1–9, 2016.

S Heinemann, Richard Wirth, and Georg Dresen. Synthesis of feldspar bicrystals by direct bonding. *Physics and Chemistry of Minerals*, 28(10):685–692, 2001.

Katharina Hartmann, Richard Wirth, and Wilhelm Heinrich. Synthetic near $\sigma 5$ (210)/[100] grain boundary in yag fabricated by direct bonding: structure and stability. *Physics and Chemistry of Minerals*, 37(5):291–300, 2010.

Diana Avadanii, Lars Hansen, Katharina Marquardt, David Wallis, Markus Ohl, and Angus Wilkinson. The role of grain boundaries in low-temperature plasticity of olivine revealed by nanoindentation. *Authorea Preprints*, 2022. doi:doi.org/10.1002/essoar.10512783.1.

JM Wheeler, DEJ Armstrong, W Heinz, and R Schwaiger. High temperature nanoindentation: The state of the art and future challenges. *Current Opinion in Solid State and Materials Science*, 19(6):354–366, 2015.

Ian N Sneddon. The relation between load and penetration in the axisymmetric boussinesq problem for a punch of arbitrary profile. *International journal of engineering science*, 3(1):47–57, 1965.

Anthony C Fischer-Cripps. Analysis of nanoindentation test data. In *Nanoindentation*, pages 39–75. Springer, 2011.

Mineo Kumazawa and Orson L Anderson. Elastic moduli, pressure derivatives, and temperature derivatives of single-crystal olivine and single-crystal forsterite. *Journal of Geophysical Research*, 74(25):5961–5972, 1969.

Huiyang Fei, Amit Abraham, Nikhilesh Chawla, and Hanqing Jiang. Evaluation of micro-pillar compression tests for accurate determination of elastic-plastic constitutive relations. *Journal of Applied Mechanics*, 79(6), 2012.

WB Durham and C Goetze. Plastic flow of oriented single crystals of olivine: 1. mechanical data. *Journal of geophysical Research*, 82(36):5737–5753, 1977.

Alexandre Mussi, Patrick Cordier, Sylvie Demouchy, and Claude Vanmansart. Characterization of the glide planes of the [001] screw dislocations in olivine using electron tomography. *Physics and Chemistry of Minerals*, 41(7): 537–545, 2014.

RJ Gaboriaud, M Darot, Y Gueguen, and J Woirgard. Dislocations in olivine indented at low temperatures. *Physics and Chemistry of Minerals*, 7(2):100–104, 1981.

PA Van Aken, B Liebscher, and VJ Styrsa. Core level electron energy-loss spectra of minerals: pre-edge fine structures at the oxygen k-edge. *Physics and Chemistry of Minerals*, 25(7):494–498, 1998.

Raymond Jeanloz, Thomas J Ahrens, JS Lally, GL Nord Jr, JM Christie, and AH Heuer. Shock-produced olivine glass: First observation. *Science*, 197(4302):457–459, 1977.

A Lacam, M Madon, and JP Poirier. Olivine glass and spinel formed in a laser heated, diamond-anvil high pressure cell. *Nature*, 288(5787):155–157, 1980.

Q Williams, E Knittle, R Reichlin, S Martin, and R Jeanloz. Structural and electronic properties of fe2sio4-fayalite at ultrahigh pressures: Amorphization and gap closure. *Journal of Geophysical Research: Solid Earth*, 95(B13): 21549–21563, 1990.

D Andrault, MA Bouhifd, JP Itie, and P Richet. Compression and amorphization of (mg, fe) 2sio4 olivines: An x-ray diffraction study up to 70 gpa. *Physics and Chemistry of Minerals*, 22(2):99–107, 1995.

Christopher A Thom, Lars N Hansen, Thomas Breithaupt, David L Goldsby, and Kathryn M Kumamoto. Backstresses in geologic materials quantified by nanoindentation load-drop experiments. *Philosophical Magazine*, 102(19): 1974–1988, 2022.

Erich Schmid and Walter Boas. Plasticity of crystals. 1950.

Julien Durinck, Benoit Devincre, Ladislas Kubin, and Patrick Cordier. Modeling the plastic deformation of olivine by dislocation dynamics simulations. *American Mineralogist*, 92(8-9):1346–1357, 2007.

M Darot, Y Gueguen, Z Benchemam, and R Gaboriaud. Ductile-brittle transition investigated by micro-indentation: results for quartz and olivine. *Physics of the Earth and Planetary Interiors*, 40(3):180–186, 1985.

Julia R Greer, Warren C Oliver, and William D Nix. Size dependence of mechanical properties of gold at the micron scale in the absence of strain gradients. *Acta Materialia*, 53(6):1821–1830, 2005.

Oliver Kraft, Patric A Gruber, Reiner Mönig, and Daniel Weygand. Plasticity in confined dimensions. *Annual review of materials research*, 40:293–317, 2010.

Jordan S Weaver, Nan Li, Nathan A Mara, David R Jones, Hansohl Cho, Curt A Bronkhorst, Saryu J Fensin, and George T Gray III. Slip transmission of high angle grain boundaries in body-centered cubic metals: Micropillar compression of pure ta single and bi-crystals. *Acta Materialia*, 156:356–368, 2018.

Nousha Kheradmand, Horst Vehoff, and Afrooz Barnoush. An insight into the role of the grain boundary in plastic deformation by means of a bicrystalline pillar compression test and atomistic simulation. *Acta Materialia*, 61(19): 7454–7465, 2013.

Peter J Imrich, Christoph Kirchlechner, Christian Motz, and Gerhard Dehm. Differences in deformation behavior of bicrystalline cu micropillars containing a twin boundary or a large-angle grain boundary. *Acta materialia*, 73: 240–250, 2014.

Katharina Marquardt, Gregory S Rohrer, Luiz Morales, Erik Rybacki, Hauke Marquardt, and Brian Lin. The most frequent interfaces in olivine aggregates: the gbcd and its importance for grain boundary related processes. *Contributions to Mineralogy and Petrology*, 170(4):1–17, 2015.

Hongzhan Fei, Sanae Koizumi, Naoya Sakamoto, Minako Hashiguchi, Hisayoshi Yurimoto, Katharina Marquardt, Nobuyoshi Miyajima, Daisuke Yamazaki, and Tomoo Katsura. New constraints on upper mantle creep mechanism inferred from silicon grain-boundary diffusion rates. *Earth and Planetary Science Letters*, 433:350–359, 2016.

CB Raleigh. Mechanisms of plastic deformation of olivine. *Journal of Geophysical Research*, 73(16):5391–5406, 1968.

Paul Raterron, Jiuhua Chen, Li Li, Donald Weidner, and Patrick Cordier. Pressure-induced slip-system transition in forsterite: Single-crystal rheological properties at mantle pressure and temperature. *American Mineralogist*, 92(8-9): 1436–1445, 2007.

WB Durham, C Froidevaux, and O Jaoul. Transient and steady-state creep of pure forsterite at low stress. *Physics of the Earth and Planetary Interiors*, 19(3):263–274, 1979.